The Response of Tropical Precipitation and Circulation to the Spatial Variance of the Cloud-Radiative Effect

YUANYUAN HUANG,[a] DAEHYUN KIM,[b] TOMOKI MIYAKAWA,[c] AND XIAOMING SHI[a,d]

[a] *Division of Environment and Sustainability, Hong Kong University of Science and Technology, Hong Kong, China*
[b] *School of Earth and Environmental Sciences, Seoul National University, Seoul, South Korea*
[c] *Atmosphere and Ocean Research Institute, The University of Tokyo, Kashiwa, Japan*
[d] *Center for Ocean Research in Hong Kong and Macau, Hong Kong University of Science and Technology, Hong Kong, China*

(Manuscript received 18 November 2025, in final form 29 April 2026, accepted 14 July 2026)

ABSTRACT: This study investigates the impact of the cloud-radiative effect (CRE) on tropical precipitation and circulation by varying the CRE intensity through tuning a cloud microphysics parameter in aquaplanet and zonally asymmetric simulations. When the CRE intensifies, tropical-mean precipitation increases, the Hadley cell (HC) strengthens, and HC edges shift equatorward in aquaplanet simulations, while the zonally asymmetric simulations exhibit the opposite responses. Although the subtropical eddies influence the poleward flank of the HC, the opposite tropical responses of precipitation and the HC in the zonally asymmetric simulations are primarily attributed to planetary-scale zonal convective aggregation and meridional–zonal circulation coupling due to the presence of the warm pool that breaks the zonal symmetry. Specifically, the enhanced CRE leads to stronger atmospheric radiative heating over the warm pool, which favors zonal convective aggregation with the expansion of the dry/subsidence region outside the warm pool, suppressing the convection and ascending motion there. The warm-pool radiative heating also strengthens the Walker circulation (WC), whose stronger and broader downward branches are superposed onto upward branches of the regional HC outside the warm pool, strongly suppressing the local HC strength and precipitation there. Consequently, the HC overall weakens, and tropical precipitation decreases. This study provides an alternative perspective on the mechanisms of HC changes, suggesting that the longitudinally different responses can be considered to supplement the zonally averaged analysis of the HC. Although this study is under the circumstances of cloud microphysics–induced CRE intensification, it offers potential insights into explaining the HC weakening in a future warming climate.

KEYWORDS: Hadley circulation; Walker circulation; Precipitation; Cloud radiative effects; General circulation models

1. Introduction

The cloud-radiative effect (CRE) is a broad and integrative concept describing the influence of clouds on radiative fluxes through their modulation of absorption, reflection, and emission. It includes both longwave (LW) and shortwave (SW) components and can be defined at the top of the atmosphere, within the atmosphere, or at the surface, depending on the application. The CRE can exert different heating or cooling effects on the atmosphere and the surface, which are modulated by cloud properties such as cloud height, optical thickness, composition, and microphysical characteristics. The CRE plays a nonnegligible role in the global radiative energy balance (Hartmann and Short 1980; Harrop and Hartmann 2016b), the variability of convective systems (Kim et al. 2015; Shi et al. 2018; Ruppert et al. 2020; Fan et al. 2021), and a wide range of global and regional climate processes (Ceppi and Hartmann 2015; Li et al. 2015; Middlemas et al. 2019; Voigt et al. 2021).

Tropical CRE has caught much attention due to its strong intensity of diabatic forcing and the associated climate and weather impacts, which are evident in satellite observations and numerical simulations (Medeiros et al. 2021; Voigt et al. 2021). Intense convection, which brings heavy rainfall, frequently occurs in the tropics. The CRE and convection are in a dynamic relation throughout a convective system life cycle, forming a "radiative–convective cloud feedback" (Lebsock et al. 2010). As a result, convection and precipitation anomalies, which interact with the large-scale circulation, are strongly correlated with the CRE variation in climatological statistics, implying the important role of the CRE in the tropical climate mean states.

How do tropical precipitation and circulation respond to the CRE variation in climate models? Some studies obtained insights by analyzing model biases (e.g., Schiro et al. 2022). In some other studies, various numerical experiments were conducted to investigate this question, focusing on different perspectives of the CRE.

"Cloud locking" is a popular approach to studying the CRE via prescribing some cloud properties and removing the interannual climate variability of clouds (Middlemas et al. 2019). Chen et al. (2021) adopted such an approach and discussed the atmospheric circulation changes in response to the CRE change in a warmer climate. Apart from that, Harrop and Hartmann (2016a) presented the climate mean-state changes under an aquaplanet configuration based on the Clouds On–Off Klimate Intercomparison Experiment (COOKIE; Stevens et al. 2012) in which the CRE can be turned off by setting the clouds to be transparent to radiation. Their results show that cloud forcing increases tropical precipitation and strengthens the Hadley cell (HC) compared to the experiments without cloud forcing. Medeiros et al. (2021) compared the precipitation changes in the cloud-locking experiments run with a fully

Corresponding author: Xiaoming Shi, shixm@ust.hk

DOI: 10.1175/JCLI-D-25-0669.1

coupled climate model and the COOKIE experiments run with the Atmospheric Model Intercomparison Project (AMIP) or aquaplanet configurations. The COOKIE experiments under the AMIP configuration and the cloud-locking experiments show only modest changes in tropical precipitation, while the COOKIE experiments under the aquaplanet configuration show a consistent precipitation reduction within the deep tropics when the LW CRE is turned off. Medeiros et al. (2021) also examined the mean precipitation responses over a broad tropical domain in COOKIE experiments, considering both ocean-only grid points and all grid points across different models, and found that the precipitation response to the CRE variations is region or model dependent.

A distinctive perspective that focuses on the microphysics-induced CRE variation is shown in Huang et al. (2024). The cloud microphysics parameter called DCS sets the threshold size for cloud ice to snow autoconversion in the Morrison and Gettelman (2008) scheme. It was tuned in aquaplanet simulations to modulate the magnitude of the CRE (termed "CRE intensity") through the direct changes in cloud ice concentration. The CRE variations examined in Huang et al. (2024) are thereby primarily dominated by the LW component. They found that the tropical mean precipitation increases and the HC strengthens with the CRE intensification, consistent with the results of Harrop and Hartmann (2016a), and they suggested that the cloud-radiative-circulation feedback can explain the possible mechanism. Although the parameter DCS has been criticized for its lack of a physical basis (Eidhammer et al. 2017), it still provides an effective approach to studying how CRE variations affect the climate mean states through experiments in climate models.

When discussing the response of circulation to the CRE variation, the HC, as a dominant tropical meridional circulation, is extensively discussed (e.g., Hwang and Frierson 2013; Harrop and Hartmann 2016a; Chen et al. 2021). Additionally, the changes in the HC, including the HC strength and width, under global warming and the associated potential mechanisms consistently attract great interest and have not been well elucidated, despite the existence of numerous theoretical and experimental studies (e.g., Seo et al. 2014; Chemke and Polvani 2021; Kim et al. 2022). Exploring how the HC responds to changes in CRE intensity provides valuable insights into comprehending the HC changes under different circumstances, particularly under global warming.

In our study, we explore the tropical climate responses under variations of the CRE intensity following Huang et al's. (2024) method of varying the DCS parameter. The CRE in our study mainly refers to its radiative effects within the atmosphere, including both LW and SW components. In addition to the aquaplanet simulations as in Huang et al. (2024), which are idealized simulations without ocean dynamics, seasonality, or zonal asymmetry, we conducted additional experiments in an aquaplanet with a wavenumber-1 warm pool and an AMIP-like configuration. The differences in how tropical precipitation and large-scale circulation respond to DCS-induced CRE changes between the aquaplanet and zonally asymmetric simulations will be discussed, and the possible mechanisms will be investigated.

2. Model and methods

a. Model setup

Three groups of simulations with different model complexities were conducted using the Community Earth System Model, version 2 (CESM2). The first group (AQUA) was run under an aquaplanet configuration in the Community Atmospheric Model, version 6 (CAM6), with the prescribed, zonally uniform "QOBS" sea surface temperature (SST) pattern as defined in the aquaplanet experiment (APE) Atlas (Williamson et al. 2012), which is also documented in Medeiros et al. (2016). The maximum SST is located at the equator with a value of 27°C. The SST decreases with latitude and reaches 0°C between 60° and 90° in both hemispheres:

$$T(\lambda, \varphi) = \begin{cases} 27\left(\frac{1}{2}\right)\left\{\left[1 - \sin^2\left(\frac{90}{60}\varphi\right)\right] + \left[1 - \sin^4\left(\frac{90}{60}\varphi\right)\right]\right\}, & \text{if } |\varphi| < 60 \\ 0, & \text{if } |\varphi| \ge 60 \end{cases}, \qquad (1)$$

where φ is the latitude and λ is the longitude. The QOBS SST pattern in the AQUA simulation is shown in Fig. 1a.

The second group (WPCP) was run on the CAM6 aquaplanet with a prescribed, zonally asymmetric SST. In this simulation group, the SST pattern was modified by adding SST anomalies (T_{ano}) to the QOBS SST given in Eq. (1) (Figs. 1b,d). The SST anomalies serve to simulate a wavenumber-1 warm pool with a maximum warming of 3 K at the center of one hemisphere and a maximum 3 K cooling at the center of the other hemisphere over the equator. The T_{ano} values are calculated as follows:

$$T_{\text{ano}}(\lambda, \varphi) = \begin{cases} 3\cos^2\left(\frac{90}{60}|\varphi|\right)\sin\lambda, & \text{if } |\varphi| < 30 \\ 0, & \text{if } |\varphi| \ge 30 \end{cases}. \qquad (2)$$

The third group (F2000) was run under a configuration with full geography and prescribed SST. It is the default component set named "F2000climo." The SST pattern in the F2000 simulation is similar to the climatological mean SST pattern observed on Earth (Fig. 1c).

All simulations adopt the finite-volume dynamical core on a latitude–longitude grid with 32 hybrid sigma-pressure levels. The horizontal resolution is 1.9° × 2.5°. All of the simulations were run with the same initialization time: the year 2000, which represents the present-day run. The parameterization schemes used in our simulations are listed in Table 1. All simulations were run for 10 years, with the first 2 years discarded as spinup. Therefore, the equilibrium states were analyzed in this study. The simulation data were archived once a day.

b. Experiment design

To control the CRE intensity, a parameter in the Morrison and Gettelman (2008) cloud microphysics scheme is tuned. The parameter, named DCS, represents the size threshold for ice-to-snow autoconversion. In this scheme, cloud ice and snow are treated as separate categories: Ice particles are

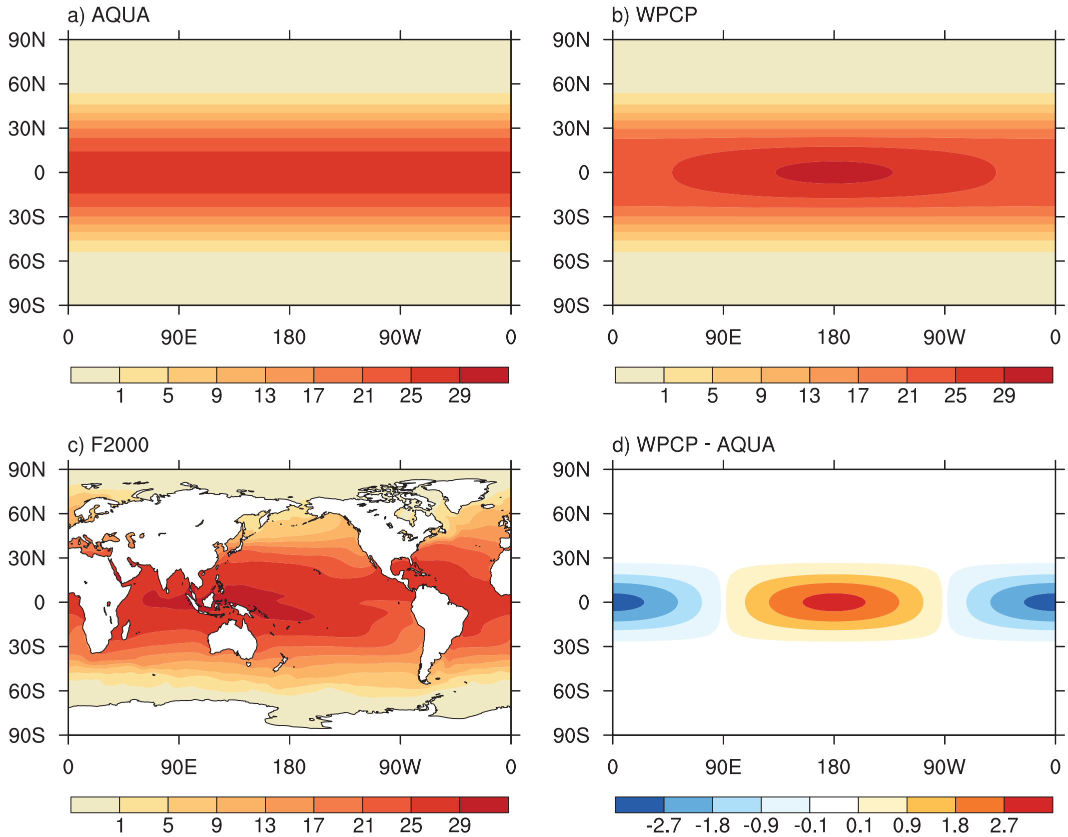

FIG. 1. (a) The prescribed global SST pattern (K) in (a) AQUA, (b) WPCP, and (c) F2000. (d) The SST difference (K) between those in WPCP and AQUA, which is the SST anomaly (T_{ano}) added to the QOBS SST pattern.

recognized as snow once they grow beyond a specified diameter. DCS directly determines the number concentration and mixing ratio of cloud ice. The size distribution is also affected by the DCS variation, but it is not directly dependent on this parameter. In this scheme, only cloud ice interacts with radiation, whereas snow is treated as a precipitating species and does not contribute to radiative transfer. We note that this distinction reflects an artificial modeling assumption rather than a physical separation in nature.

DCS has been demonstrated to be an important parameter influencing cloud-radiative feedback, convective systems, and even the climate mean state across different models (Zhao et al. 2013; Eidhammer et al. 2014; Fan et al. 2021; Zhang et al. 2025). A larger DCS delays the conversion of cloud ice to snow, allowing more cloud ice to remain in the atmosphere, whereas a smaller DCS permits this conversion to occur at smaller particle sizes of cloud ice. The increased cloud ice induced by a larger DCS traps more radiative flux within the atmosphere, leading to stronger radiative heating and consequently intensifying the CRE, while a smaller DCS corresponds to a weaker CRE. It should be noted that DCS does not directly modify latent heat release associated with phase transitions. The changes in microphysical heating arise indirectly through convection and circulation adjustments driven by DCS-induced radiative heating changes, rather than from the DCS parameter itself. Although the CRE variations are primarily dominated by the LW component, mainly due to changes in cloud ice content within high

TABLE 1. The parameterization schemes used in all simulations.

Process	Scheme name	Reference
Deep convection	ZM	Zhang and McFarlane (1995)
Cloud microphysics	GM2	Gettelman and Morrison (2015)
Boundary layer turbulence	Cloud layers unified by binormals (CLUBB)	Golaz et al. (2002) Bogenschutz et al. (2013)
Shallow convection		
Cloud macrophysics		
Radiative transfer	Rapid Radiative Transfer Model for general circulation models (RRTMG)	Iacono et al. (2008)

clouds, the SW CRE also varies with DCS variations. Therefore, we focus on the total atmospheric CRE in this study. In our experiments, two simulations were run with DCS = 500 μm (DCS500) and DCS = 200 μm (DCS200), respectively.

c. *Meridional and zonal circulation*

1) Hadley cell

The meridional mass streamfunction (MMSF) quantifies the mean meridional atmospheric circulation, which is defined by integrating the northward mass flux above a particular pressure level as follows:

$$\psi_{\mathrm{HC}}(t, p, x) = \frac{2\pi a \cos\phi}{g} \int_p^{p_{\mathrm{sfc}}} [v] dp, \tag{3}$$

where ψ_{HC} is the zonally averaged MMSF, a is the radius of Earth, g is the gravitational acceleration, p is the pressure, p_{sfc} is the surface pressure, $[v]$ is the zonal-mean meridional wind, and ϕ is the latitude in radians.

The HC strength is quantitatively calculated as the maximum of the absolute value of ψ_{HC} at 500 hPa near the HC center in each hemisphere ($\psi_{\mathrm{HC}}^{\max}$). The HC edge is defined as the location of $\psi_{\mathrm{HC}} = 0$ at 500 hPa over the subtropics.

2) Regional Hadley cell

Different from the aforementioned calculation of MMSF for the global HC, the calculation of regional MMSF (RMMSF) for the regional HC along the longitudes requires the consideration of the irrotational component decomposed from the horizontal wind (Zhang and Wang 2013, 2015; Li et al. 2023), shown as follows:

$$\psi_{\mathrm{RHC}}(t, p, x, y) = \frac{2\pi a \cos\phi}{g} \int_p^{p_{\mathrm{sfc}}} v_d dp, \tag{4}$$

where ψ_{RHC} is the RMMSF and v_d represents the divergent component of meridional wind.

3) Walker circulation

The zonal equatorial circulation can be represented as the zonal mass streamfunction (ZMSF). Following Yu and Zwiers (2010), it can be calculated as follows:

$$\psi_{\mathrm{WC}}(t, p, y) = \frac{2\pi a}{g} \int_p^{p_{\mathrm{sfc}}} u_d dp, \tag{5}$$

where ψ_{WC} is the equatorial ZMSF and u_d is the divergent component of the zonal wind averaged over the deep tropics (5°S–5°N).

3. General climate responses: Zonal-mean perspective

a. *Precipitation and cloud forcing*

The meridional profiles of precipitation in all simulations are shown in Fig. 2a. Both AQUA and F2000 exhibit a double intertropical convergence zone (ITCZ) with two precipitation peaks on both sides of the equator, while WPCP only simulates a single ITCZ. When DCS increases, the precipitation across the ITCZ increases significantly in AQUA, and the ITCZ contracts toward the equator. However, in WPCP, the tropical precipitation decreases overall with the increasing DCS, despite having minimal changes at the equator. The tropical precipitation in F2000 also shows an opposite response relative to that in AQUA, characterized by a hemisphere-asymmetric response with a more significant decrease around the Northern Hemisphere (NH) ITCZ relative to the change in the Southern Hemisphere (SH). Figure 2c shows the mean precipitation within 5°S–5°N and its fractional changes from DCS200 to DCS500, reflecting the opposite precipitation responses to the CRE intensification between AQUA and zonally asymmetric simulations. The specific mean precipitation values are documented in Table A2 in appendix A. The mean precipitation within 10°S–10°N also exhibits a similar opposite response (Table A1).

In AQUA, the strong precipitation increase over the tropics is mostly offset by the subtropics, inferred from Fig. 2a (specific calculations are not shown). In WPCP and F2000, the magnitudes of the precipitation responses over the tropics and subtropics are small compared to those in AQUA. This is likely because the zonally uniform AQUA generates strong meridional circulation, strengthening the gradient of precipitation distribution, while the zonally asymmetric responses in WPCP and F2000 weaken this effect, which will be discussed later.

The larger DCS value is associated with stronger CRE, which can be reflected in the LW cloud forcing changes. In the three groups of simulations, the zonal-mean LW cloud forcing increases with increasing DCS (Fig. 2b). The averaged LW cloud forcing over the deep tropics (5°S–5°N) and its fractional change from DCS200 to DCS500 are shown in Fig. 2d. The positive LW cloud forcing anomalies imply a stronger cloud-induced LW radiative heating in the atmosphere, which mostly results from more cloud ice in high clouds due to the varied DCS. The stronger radiative heating warms the tropical troposphere, leading to a higher air temperature (Fig. 6), which will be further discussed in section 3c.

In addition, from the energetic perspective, global-mean precipitation is balanced by global-mean atmospheric radiative cooling (Stephens and Ellis 2008; Allen and Ingram 2002). This global energy balance framework is also reflected in our simulations, where the decrease in global-mean precipitation scales with the reduction in global-mean atmospheric radiative cooling (detailed calculations not shown). However, the global energy balance does not determine the spatial precipitation distribution, and regional precipitation responses are strongly modulated by energy transport and circulation changes. In the next section, we diagnose the meridional circulation responses under CRE intensification.

b. *Meridional circulation*

1) Hadley cell

The tropical mean precipitation and ITCZ are closely associated with atmospheric general circulation, especially the HC, the dominant meridional large-scale circulation. Figure 3 shows the climatological zonal-averaged MMSF, ψ_{HC}, changes

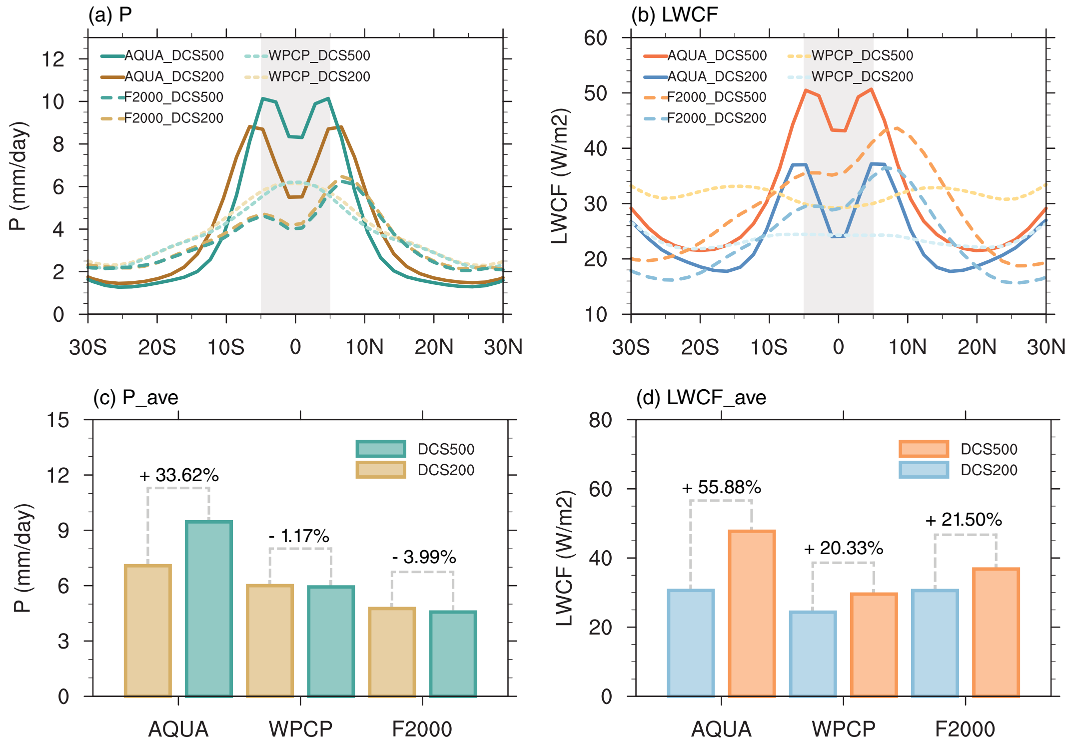

FIG. 2. (a) The climatological zonal-averaged precipitation (P; mm day^{-1}) in all simulations. (b) As in (a), but for the LW cloud forcing (LWCF; W m^{-2}). (c) The mean precipitation over the deep tropics (5°S–5°N). (d) As in (c), but for the LWCF. The percentages on top of the bars in (c) and (d) are the fractional changes from DCS200 to DCS500.

from DCS200 to DCS500. In AQUA (Fig. 3a), when the CRE intensifies, the axisymmetric HC becomes stronger, represented by a positive/negative ψ_{HC} anomaly over the tropics in the NH/SH. The stronger HC with stronger upward motion over the tropics provides a favorable dynamic condition for deep convection. The possible mechanism for the HC strengthening and tropical precipitation increase in AQUA can be explained by a cloud-radiative-circulation feedback (Huang et al. 2024). In this feedback, changes in cloud microphysics enhance radiative heating over the equator, which in turn strengthens meridional heat transport, driving a stronger HC. However, the HC in WPCP and F2000 overall weakens under the stronger CRE (Figs. 3b,c), opposite to those in AQUA. The HC strength $\psi_{\mathrm{HC}}^{\max}$ (defined in section 2c) and its fractional change from DCS200 to DCS500 in Figs. 4a–c also support the opposite HC changes in AQUA and zonally asymmetric simulations.

Note that the climatological ψ_{HC} has regional variations with latitudes, which are more significant in WPCP and F2000 (Figs. 3b,c). In WPCP and F2000, the equatorward flank of the HC weakens, and the poleward flank of the HC strengthens in both hemispheres with opposite ψ_{HC} anomalies in the upward and downward branches of the HC.

The HC edges also shift in response to CRE variations. Comparison of the black and gray contours in Fig. 3 shows that CRE intensification leads to a contraction of the HC with equatorward-shifted HC edges in AQUA, whereas the HC edges shift poleward in WPCP and F2000. Specifically, the subtropical locations where $\psi_{\mathrm{HC}} = 0$ at 500 hPa define the HC edges. Figures 4d–l further illustrate the opposite HC edge shifts in AQUA and zonally asymmetric simulations. Quantitatively, the HC edges in AQUA shift equatorward by 0.27° latitude on average across both hemispheres, while those in WPCP and F2000 shift poleward by 0.46° and 0.58° latitude, respectively. The less than 1° HC shifts are still significant and comparable to previous studies (Seo et al. 2023; Kim et al. 2023).

Although the changes in HC strength and the HC edge may depend on different mechanisms, many previous studies have found that a weakened HC is associated with a poleward-shifted HC edge, which is similar to the circumstance in our simulations. Such HC changes are particularly found under greenhouse gas (GHG)-induced global warming (e.g., Lu et al. 2008; Hu et al. 2018; Chemke et al. 2019).

2) EDDY ACTIVITIES

One classic theory based on the zonal momentum balance in the upper troposphere explains how eddy activities link to the changes in HC strength and HC edge (Walker and Schneider 2006; Schneider and Bordoni 2008; Levine and Schneider 2011; Seo et al. 2023). In the upper troposphere, the friction and the vertical momentum advection by the mean circulation can be neglected. The mean zonal momentum balance in a statistically steady state is approximately

$$(f + \overline{\zeta})\overline{v} = f(1 - \mathrm{Ro})\overline{v} \approx S, \tag{6}$$

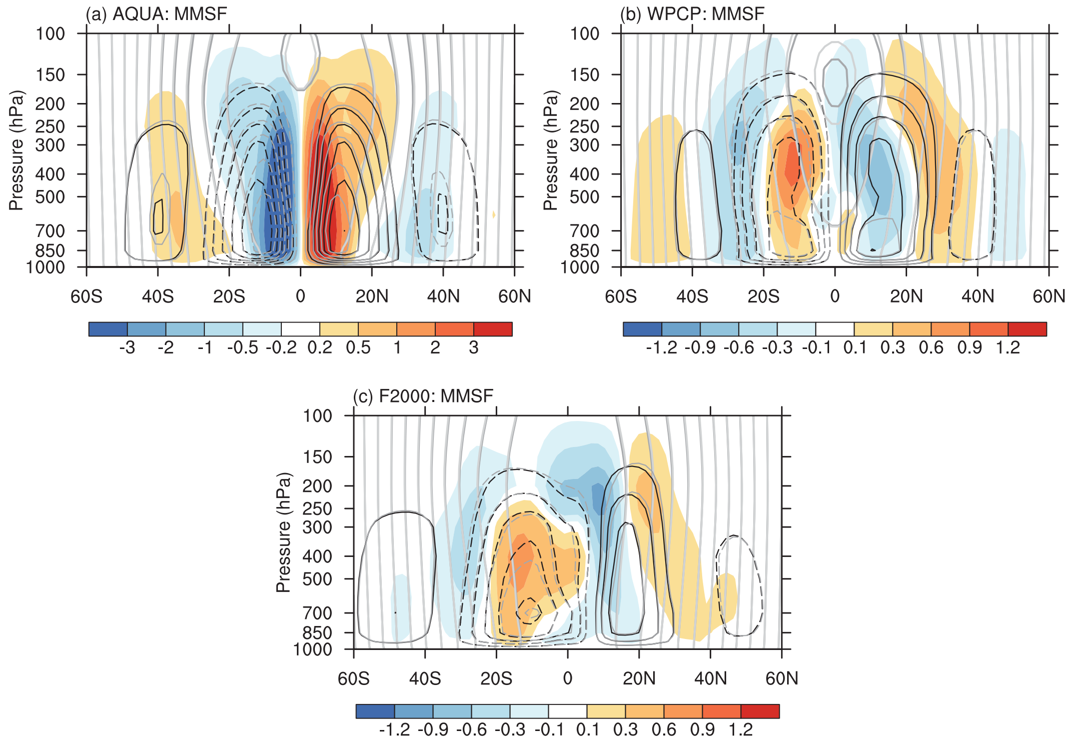

FIG. 3. (a) The difference in the climatological zonal-averaged meridional mass streamfunction (ψ_{HC}, color; 10^{10} kg s^{-1}) between DCS500 and DCS200 in AQUA. The climatological ψ_{HC} for DCS200 and DCS500 is overlaid by the black thin contour and gray thin contour, respectively. The dashed contour indicates negative values. The positive (negative) ψ_{HC} represents the clockwise (counterclockwise) circulation. The contour equal to zero is masked. The overlaid thick gray contour represents the absolute angular momentum (light gray is for DCS200 and dark gray is for DCS500; contour interval is $\Omega a^2/15$; Ω is the angular velocity, and a is the radius of Earth). (b) As in (a), but for WPCP. (c) As in (a), but for F2000. The contour interval of climatological ψ_{HC} is 3×10^{10} kg s^{-1} in (a) and 2×10^{10} kg s^{-1} in (b) and (c).

where f is the planetary vorticity (Coriolis parameter), ζ is the relative vorticity, υ is the meridional wind, $\mathrm{Ro} = -\overline{\zeta}/f$ is the local Rossby number, and $S = \partial_y(\overline{u^*\upsilon^*}\cos\phi)$ is the horizontal eddy momentum flux divergence (EMFD), where u is the zonal wind and ϕ is the latitude in radians. The absolute vorticity $f + \overline{\zeta} = -(a^2\cos\phi)^{-1}\partial_\phi\overline{m}$ is proportional to the meridional gradient of the absolute angular momentum per unit mass ($\overline{m}$), where a is Earth's radius. The overbars denote the temporal and zonal mean, and the asterisks denote the zonal deviation.

When $\mathrm{Ro} \to 1$, the absolute angular momentum contours are horizontal, and the EMFD approaches zero ($S \to 0$), which means the meridional mean circulation is decoupled from EMFD, and HC is thermally driven. In the limit $\mathrm{Ro} \to 0$, the absolute angular momentum contours are vertical, and $\overline{\upsilon} \approx S/f$ indicates that EMFD plays an important role. Around the HC edge (or the poleward boundary of the HC), the Ro is small ($\overline{\upsilon} \approx S/f$), which implies that the location of the HC edge is associated with the location of zero crossing of EMFD, and the stronger EMFD over the upper branch of the HC is associated with a stronger meridional overturning circulation.

Comparing the absolute angular momentum contours with the MMSF contours in Fig. 3, we could find that the angular momentum tends to conserve in the upper branches of the HC in AQUA, indicating weak eddy effects on the HC, while the more vertical angular momentum contours significantly cross the MMSF contours in the upper branches of the HC in WPCP and F2000, indicating the HC is affected by stronger eddy effects. Such differences between AQUA and zonally asymmetric simulations can also be reflected in the magnitudes of HC edge shifts in Figs. 4g–l, where the HC edges show stronger shifts in WPCP and F2000 relative to AQUA. The changes in absolute angular momentum from DCS200 to DCS500 (figure not shown) show an increase at the subtropics in AQUA, while concentrating at the tropics in WPCP and F2000. This is because a stronger HC transports angular momentum to higher latitudes, while angular momentum accumulates in the tropics when HC is weak.

Our simulation results show the close relationship between EMFD and HC changes under CRE intensification (Fig. 5). The climatological zonal-averaged EMFD peaks at around 20°N/S in all simulations. In AQUA, there exist positive EMFD anomalies at 10°N/S when DCS increases (Fig. 5a), indicating that the EMFD and zero crossing of EMFD shift equatorward, consistent with the contracted HC and the larger $|\psi_{HC}|$ on the equatorward flank of the HC. In contrast, the positive EMFD anomalies in WPCP and F2000 show a poleward shift compared to the climatological EMFD centers (Figs. 5b,c), consistent with the poleward-shifted HC edges and the larger $|\psi_{HC}|$ on the

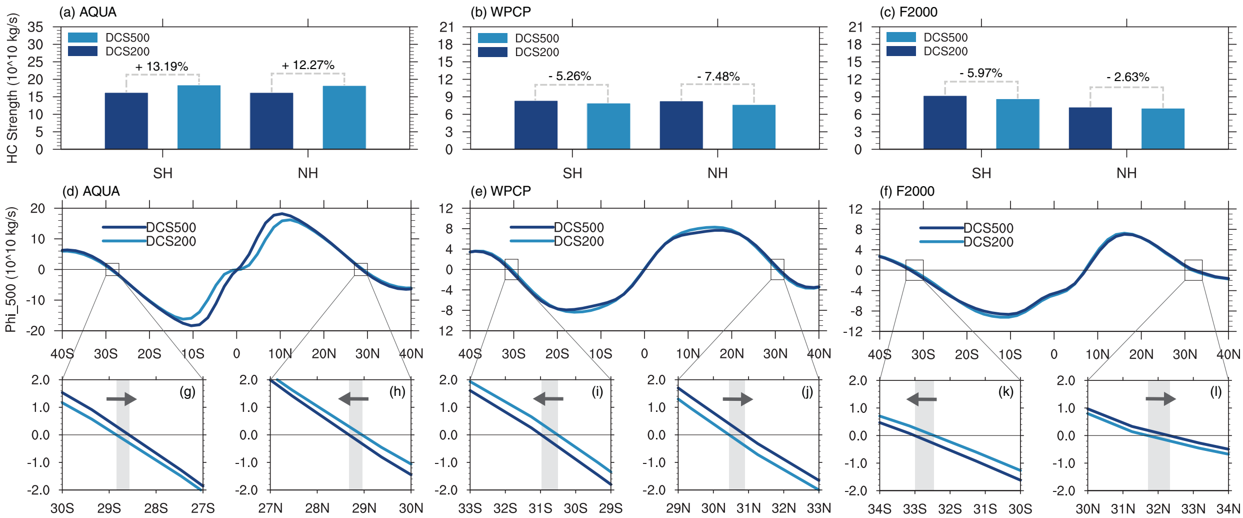

FIG. 4. (a) The HC strength (ψ_{HC}^{max}, 10^{10} kg s^{-1}) of AQUA in the two hemispheres. The percentages on top of the bars are the fractional changes from DCS200 to DCS500. (b) As in (a), but for WPCP. (c) As in (a), but for F2000. (d) The latitudinal changes in the climatological zonal-averaged meridional mass streamfunction (ψ_{HC}; 10^{10} kg s^{-1}) at 500 hPa in AQUA. The location of $\psi_{HC} = 0$ at 500 hPa over the subtropics represents the HC edges. (e) As in (d), but for WPCP. (f) As in (d), but for F2000. (g)–(l) The amplification of (d)–(f) around the HC edges. The black arrows represent the moving directions of the HC edges from DCS200 to DCS500.

poleward flank of the HC. At the equatorward flank of the HC in WPCP and F2000, the anomalous convergence of eddy momentum flux there contriutes to the weaker circulation.

The Eliassen–Palm flux (EPF) changes in Fig. 5 represent the eddy activity changes over the subtropics to the extratropics under the CRE intensification, which mainly influence the poleward flank of the HC. Due to the HC terminating at the subtropics (around 30°N/S), we only focus on the EPF around 30°N/S, which is most closely related to the HC edge changes. In AQUA (Fig. 5a), when CRE intensifies, the upward EPF anomalies over the subtropics indicate stronger eddy heat activities and the stronger baroclinic instability over the subtropics, which is demonstrated to be associated with the HC edge equatorward shift as the HC terminates at the baroclinic zone (Seo et al. 2023). Instead, the weakened EPF in the midtroposphere in WPCP and F2000 reflects weaker eddy activities (red boxes) with anomalous equatorward eddy heat flux, associated with weaker baroclinic instability. In this case, the baroclinic zones shift poleward, and the HC edges also shift poleward. These opposite eddy activity responses over the subtropics are associated with the opposite meridional temperature gradient between the tropics and subtropics, which will be discussed in Fig. 7.

Despite the subtropical eddies playing a crucial role in affecting the HC characteristics, particularly at the poleward flank of the HC, the contributions of those subtropical eddies to the changes in the entire HC are difficult to quantify, as most previous studies preferred to explain this issue qualitatively. In addition, many other factors are proposed to be important to the changes in HC strength, such as static stability, tropopause height, and diabatic forcing (e.g., Seo et al. 2014; Chemke and Polvani 2021; Kim et al. 2022). However, it is still difficult to find a unified or universal theory to explain the mechanisms of HC changes (especially the HC strength changes), combining all those key factors together, not only in our simulations but also in other studies. Thus, other possible perspectives will be discussed in this study to help us understand the interesting HC responses and their associated tropical precipitation responses under the CRE intensification in our simulations.

It is worth mentioning that most theories focus on the general HC strength changes and do not pay much attention to the latitudinal variations of the HC. The latitudinal variations are represented as the opposite responses at the equatorward and poleward flanks of the HC observed in our simulations. Given that the HC responses at the equatorward flank contribute most to the HC strength, and the opposite responses (including the HC and the tropical mean precipitation) between AQUA and zonally asymmetric simulations under the CRE intensification dominate in the tropics, the tropical processes, such as the tropical diabatic forcing and other dynamic processes, should be further analyzed. Over the tropics, the eddy effects become insignificant (Walker and Schneider 2006; Schneider and Bordoni 2008), which will not be considered.

c. *Temperature, moisture, and cloud fraction*

Based on the analyses above, the key finding of this study is the opposite tropical responses of mean precipitation and the HC to CRE intensification between the aquaplanet and zonally asymmetric simulations. In this section, we diagnose the general condition responses, including temperature, moisture, and cloud fraction, to assess whether large-scale thermodynamic changes can account for these opposite precipitation and HC responses.

The global mean-state changes in temperature, moisture, and cloud fraction in our simulations are shown in Fig. 6. The tropical troposphere exhibits the most significant temperature response to the DCS-induced CRE intensification, particularly in the upper troposphere (Figs. 6a–c). The tropical

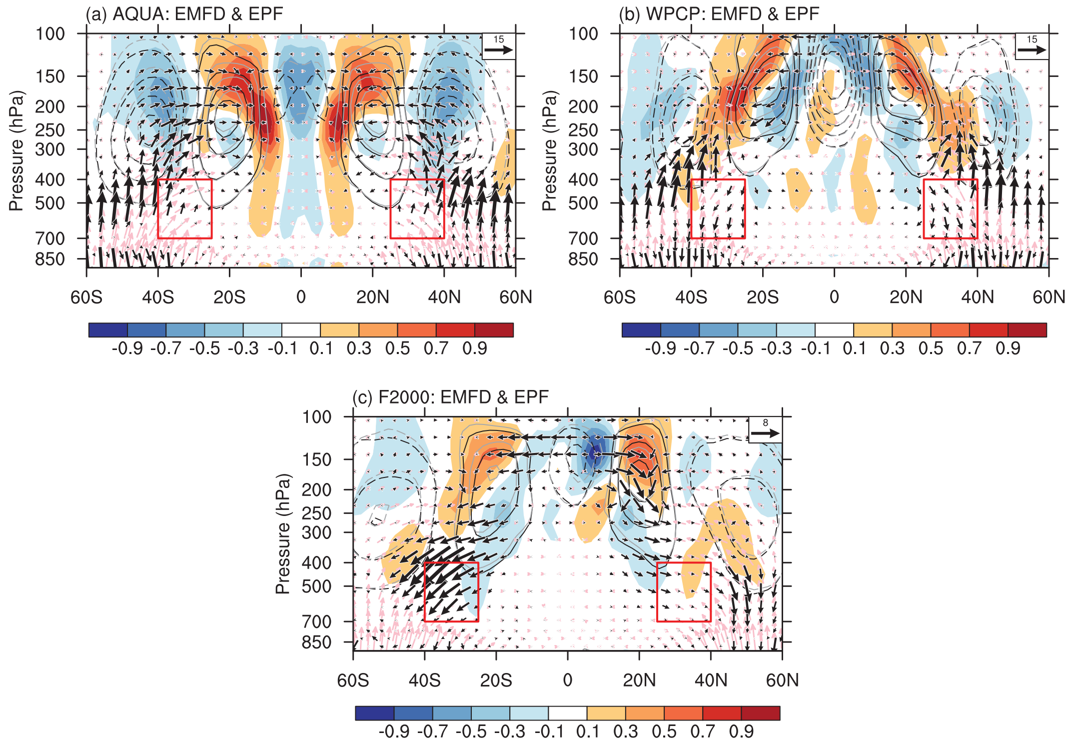

FIG. 5. (a) The climatological zonal-averaged horizontal EMFD $\partial_y(\overline{u^*v^*}\cos\phi)$ (contour; m s^{-1} day^{-1}) of DCS200 (black contour) and DCS500 (gray contour), and the difference in the climatological zonal-averaged EMFD (color) between DCS500 and DCS200 in AQUA. The climatological zonal-averaged EPF (pink vector; m^2 s^{-2}) of DCS200 and the difference in the EPF (black vector) between DCS500 and DCS200. The EPF is scaled by $\sqrt{1000/p}$. The contour interval is 1 m s^{-1} day^{-1}. The dashed contour indicates negative values. The positive (negative) EMFD represents the divergence (convergence). The contour equal to zero is masked. The red boxes indicate the regions over 700–400 hPa within 25°–40°. (b) As in (a), but for WPCP. (c) As in (a), but for F2000.

atmosphere is dominated by high clouds (contours in Figs. 6g–i), which are closely associated with frequent and intense deep convection. These high clouds, containing abundant cloud ice, are sensitive to DCS variations. Under the CRE intensification, the changes in high cloud fraction (shading in Figs. 6g–i) enhance radiative heating, while deep convection provides strong latent heating, together contributing to the strong warming in the upper tropical troposphere. In addition, the tropopause becomes higher when DCS increases. Compared with the other two groups of simulations, the AQUA simulations exhibit a larger warming amplitude, with the maximum temperature increase exceeding 2 K.

Such a warming pattern in these simulations shares some similarities with GHG-induced global warming (e.g., Shaw 2019), such as the warming over the tropical troposphere and the cooling over the stratosphere. In the more realistic F2000 experiment (Fig. 6c), a near-surface cooling is evident over the Arctic, in contrast to the so-called “Arctic amplification” typically observed under GHG-induced global warming. Consistently, the surface net LW radiative response to CRE intensification also exhibits a cooling effect over the Arctic (figure not shown). The different albedo and cloud-radiative feedback caused by DCS variations in F2000 may help explain the opposite and indicate that the cloud process–induced global warming examined here is driven by different mechanisms than GHG-induced warming, which requires further investigation.

In the upper troposphere (above 300 hPa), the meridional temperature gradient significantly increases in all simulations under the CRE intensification. In the midtroposphere (around 450–600 hPa), the meridional temperature gradient also generally increases when comparing the tropics with the midlatitudes, while it exhibits different responses to the CRE intensification between the tropics and the subtropics. For a clearer comparison, the latitudinal profiles of the midtropospheric (averaged over 450–600 hPa) air temperature responses to CRE intensification are shown in Fig. 7. From the tropics to the midlatitudes, the air temperature anomalies are positive in all simulations. The warming over the tropics is much stronger than that over the subtropics in AQUA, implying a stronger meridional temperature gradient. On the contrary, the warming becomes stronger over the subtropics (peaking around 30°S/N) in WPCP and F2000, indicating a weaker meridional temperature gradient. These opposite meridional temperature gradient responses explain the opposite eddy activity and baroclinic responses over the subtropics (Fig. 5). Although the global meridional temperature gradient increases overall (Figs. 6a–c), the opposite responses in the midtroposphere from the tropics to the subtropics (Fig. 7)

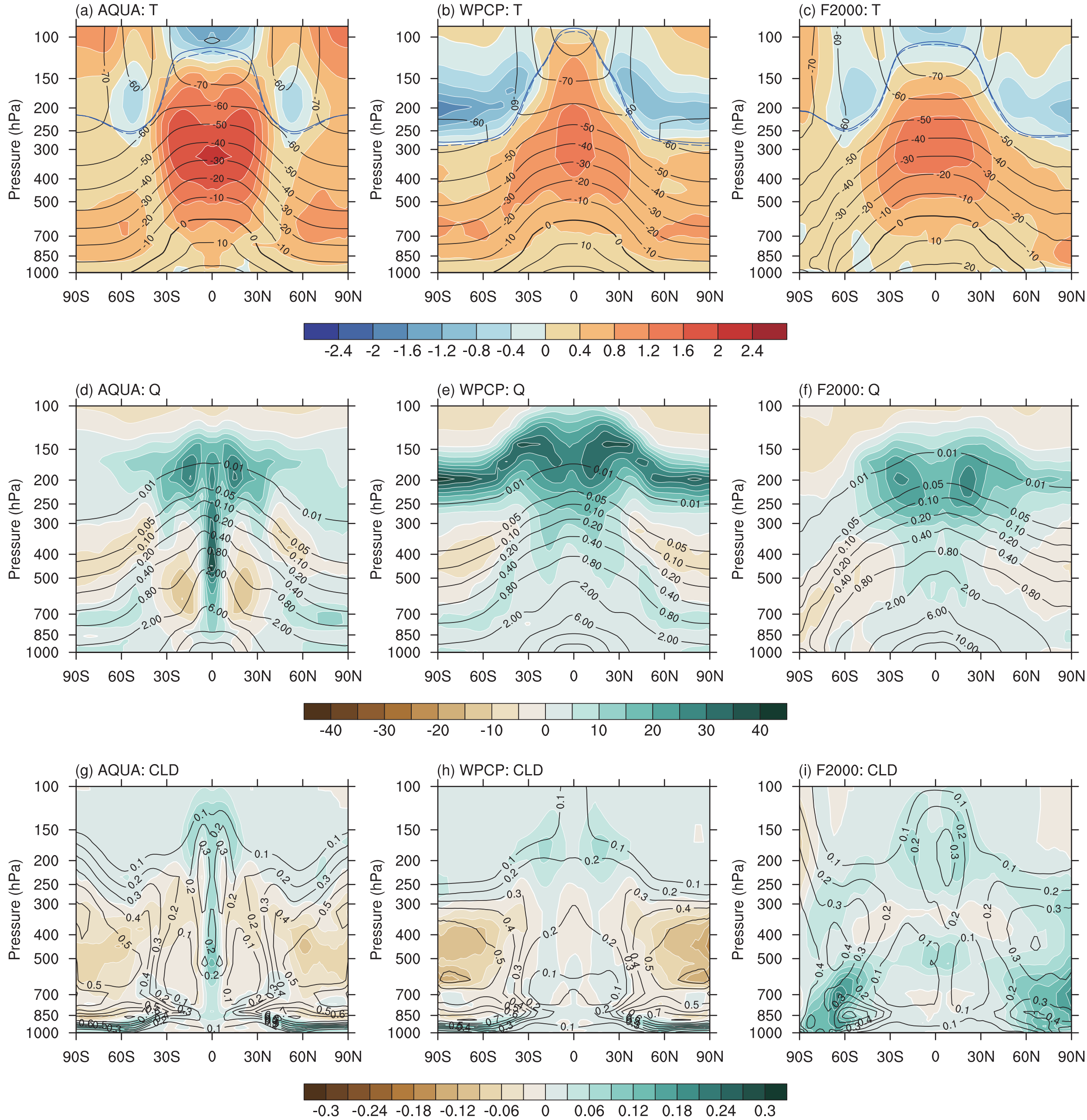

FIG. 6. (a) The climatological zonal-averaged air temperature (T, contour; °C) of DCS200 and the difference in the climatological zonal-averaged T (color) between DCS500 and DCS200 in AQUA. The overlaid blue curves represent the tropopause (solid curves: DCS500; dashed curves: DCS200). (b),(c) As in (a), but for WPCP and F2000, respectively. (d) The climatological zonal-averaged specific humidity (Q, contour; g kg^{-1}) of DCS200 and the fractional changes in the climatological zonal-averaged Q (color, %) from DCS200 to DCS500 in AQUA. (e),(f) As in (d), but for WPCP and F2000, respectively. (g) The climatological zonal-averaged cloud fraction (CLD, contour) of DCS200 and the difference in the climatological zonal-averaged CLD (color) between DCS500 and DCS200 in AQUA. (h),(i) As in (g), but for WPCP and F2000, respectively.

display the different climate states between AQUA and zonally asymmetric simulations, at least regionally.

As to the moisture changes in our simulations (Figs. 6d–f), the tropical atmosphere becomes moister throughout the troposphere with positive fractional changes as DCS increases in all simulations. The moisture in the higher troposphere exhibits larger fractional changes, implying that deep convection strengthens when DCS increases.

With increasing DCS, the tropical atmosphere becomes warmer and moister in all simulations, as discussed above.

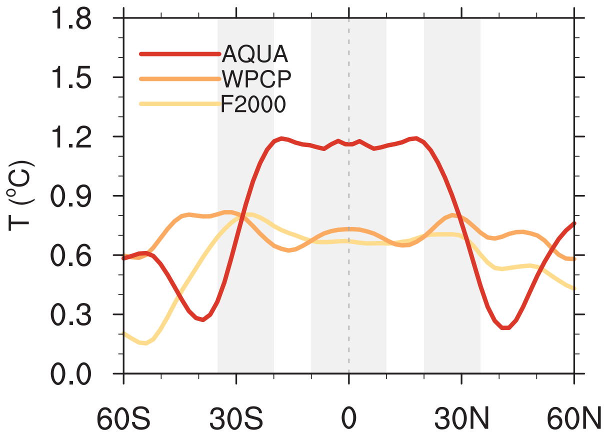

FIG. 7. The difference in the climatological zonal-averaged air temperature (T, °C) between DCS500 and DCS200 in the midtroposphere (averaged around 450–600 hPa). The gray areas indicate the regions of the tropics and subtropics.

However, the associated temperature change (more warming in the upper troposphere) is indeed an unfavorable condition for deep convection, as it increases static stability. In the equilibrated AQUA state, tropical precipitation nevertheless increases with higher DCS, implying that convection can be sustained despite the enhanced static stability under stronger DCS forcing. In contrast, the zonally asymmetric simulations exhibit different precipitation responses from AQUA, suggesting that other processes may play a dominant role. In the next section, the zonally asymmetric responses in WPCP and F2000 are examined in more detail, providing insights that cannot be captured from a zonal-mean perspective.

4. Zonally asymmetric responses

According to the experiment design, the zonal asymmetry in WPCP is due to the existence of the warm pool, and that in F2000 is additionally affected by the land–sea distribution and land processes. In the following subsections, the zonally asymmetric responses in WPCP and F2000 will be further investigated, which may help us to understand the reasons for the opposite tropical responses.

a. Planetary-scale convective aggregation

In AQUA, spatial changes in precipitation between two varying DCS experiments are generally quasi uniform with minimal zonal variability (Fig. 8a). In WPCP (Fig. 8b), anomalous precipitation exhibits a Matsuno–Gill response pattern. The tropical precipitation increases around the warm pool region (slightly ahead of its center) and decreases outside the warm pool, particularly to the west of it. Comparison of the climatological and anomalous precipitation shows a contraction of the heavy precipitation region toward the warm pool, accompanied by an expansion of the dry region. Over the tropics (10°S–10°N), the area with precipitation greater than 6 mm day^{-1} decreases by 7.29% from DCS200 to DCS500, while the area with precipitation less

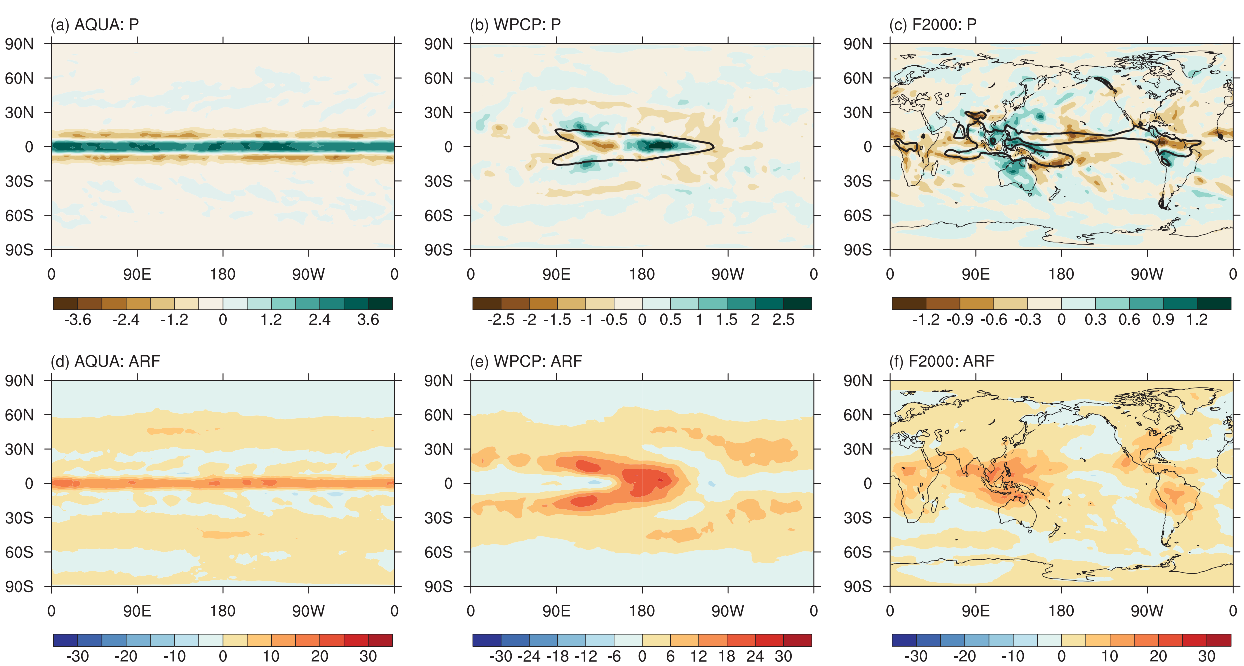

FIG. 8. (a) The difference in the climatological precipitation (color; mm day^{-1}) between DCS500 and DCS200 in AQUA. (b) As in (a), but for WPCP. (c) As in (a), but for F2000. In (b) and (c), the climatological precipitation contours of DCS200 are overlaid as a reference. The encircled regions represent precipitation larger than 6 mm day^{-1}. (d) The difference in the climatological ARF (color; W m^{-2}) between DCS500 and DCS200 in AQUA. The ARF is calculated as the difference between the net radiative fluxes (SW + LW) at the top of the atmosphere and at the surface, without subtracting the clear-sky component. (e) As in (d), but for WPCP. (f) As in (d), but for F2000. The positive values mean the radiative heating anomaly.

than 3 mm day^{-1} increases by 19.27%. Similarly, in F2000 (Fig. 8c), tropical precipitation mainly increases around the warm pool and decreases outside the warm pool (such as in the central–eastern Pacific and the western Indian Ocean) when DCS increases. The shrinkage of the heavy precipitation region and the expansion of the dry region are also evident, further supported by a 3.62% decrease in the area with precipitation greater than 6 mm day^{-1} and a 13.11% increase in the area with precipitation less than 1 mm day^{-1} over the tropics.

The longitudinal differences in tropical precipitation responses account for the small amplitudes of zonal-mean precipitation changes under CRE intensification in WPCP and F2000 (Figs. 2a,c). The negative fractional changes in tropical mean precipitation in both WPCP and F2000 are primarily driven by a reduction in precipitation outside the warm pool, which offsets the increase within it. Specifically, calculations for the tropics (10°S–10°N) show that in WPCP, precipitation over the warm pool (135°E–135°W) increases by 3.84% from DCS200 to DCS500, while precipitation outside the warm pool decreases by 9.56%; in F2000, precipitation over the warm pool (90°E–180°) increases by 1.47%, whereas precipitation outside the warm pool decreases by 6.85%.

Regarding the general atmospheric radiative responses to the CRE intensification, the atmospheric radiative forcing (ARF) (including both LW and SW components) is shown in Figs. 8d–f. Unlike the quasi-zonally uniform anomalous radiative heating observed over the deep tropics, WPCP and F2000 exhibit zonally asymmetric radiative responses. In WPCP, the significant Matsuno–Gill response pattern is driven by the anomalous heat source induced by the increased DCS, while it is not significant in F2000. Within the tropics, the anomalous radiative heating over the warm pool in WPCP and F2000 indicates that the regions with frequent and intense deep convection are more sensitive to DCS variations. The overall distribution patterns of atmospheric radiative forcing responses (Figs. 8d–f) are primarily contributed by atmospheric cloud radiative forcing changes, rather than by the changes in other radiative processes observed in the clear-sky component (Fig. B1 in appendix B). However, the anomalous radiative cooling from the clear-sky component overwhelms the weak anomalous cloud radiative heating outside the warm pool, leading to net anomalous tropical radiative cooling outside the warm pool in WPCP and F2000.

Similar to the atmospheric radiative heating responses, the tropical cloud fraction responses in the zonal direction (Figs. 9e,f) also suggest that the warm pool, with more ice-containing high clouds, is more sensitive to DCS variations. Although an increase in DCS cannot directly generate new clouds in regions lacking cloud ice, it can still influence the regions with little clouds outside the warm pool through diffusion and circulation adjustments. These indirect effects ultimately emerge in the equilibrium state, leading to weak increases in high cloud fraction outside the warm pool when DCS increases.

The zonal asymmetric tropical responses in WPCP and F2000 are also shown by the vertical distributions of tropical vertical velocity and relative humidity in Fig. 9. In both WPCP and F2000, there is an upward motion anomaly over the warm pool, while the downward motion anomaly dominates outside the warm pool. The downward motion anomaly outside the warm pool has a stronger or comparable intensity and a wider range relative to the upward motion anomaly. The stronger upward motion over the warm pool is associated with the stronger convection there (Figs. 8b,c), and the wider anomalous downward motion outside the warm pool suppresses the convection, corresponding to the dry (or subsidence) region expansion. The relative humidity responses to the CRE intensification in Figs. 9c and 9d also show opposite responses between the warm pool and the region outside the warm pool. The troposphere over the warm pool becomes moister, while the midtroposphere outside the warm pool becomes drier.

According to the above analysis, the tropical responses to CRE intensification in WPCP and F2000 exhibit planetary-scale convective aggregation in the zonal direction, characterized by convective region shrinkage, dry/subsidence region expansion, a drier midtroposphere, and anomalous radiative cooling outside the warm pool. Due to the absence of zonal asymmetry, AQUA does not show a zonal convective aggregation, despite exhibiting meridional narrowing of the convective region (Figs. 2a and 8a).

The planetary-scale convective aggregation identified in WPCP and F2000 shares qualitative similarities with environmental features reported in previous observational and modeling studies of convective aggregation, such as drier conditions and enhanced radiative cooling outside convective regions (Tobin et al. 2012, 2013; Arnold and Randall 2015). Notably, studies such as Tobin et al. (2012, 2013) primarily examine convective aggregation at the synoptic or mesoscale, whereas the aggregation discussed in our study emerges at the planetary scale, and thus the underlying mechanisms and experimental frameworks are not necessarily identical. In addition, Arnold and Randall (2015) and Fan et al. (2021) highlight the important role of radiative feedbacks in shaping the convective aggregation, which is also relevant to our results. For example, Arnold and Randall (2015) found that eliminating the LW radiative feedback (homogenized LW heating) weakens the planetary-scale convective aggregation. This is suggestive of our experimental results: Stronger atmospheric radiative heating over the warm pool in WPCP and F2000 promotes planetary-scale convective aggregation, particularly in the zonal direction. The dry/subsidence region expansion outside the warm pool thereby suppresses the convection and ascending motion there.

In addition, when the DCS is fixed, introducing a warm pool in WPCP facilitates zonal large-scale convective aggregation, which is broadly consistent with the results of Quan et al. (2025): An increase in the east–west SST gradient strengthens large-scale convective aggregation. The potential role and mechanisms of the zonal SST gradient in modulating CRE-convective aggregation interactions remain an interesting topic for further investigation.

b. *Coupling of the Hadley cell and Walker circulation*

1) WALKER CIRCULATION

Unlike the zonally symmetric AQUA, the more complex zonal asymmetric responses (e.g., diabatic forcing) in WPCP

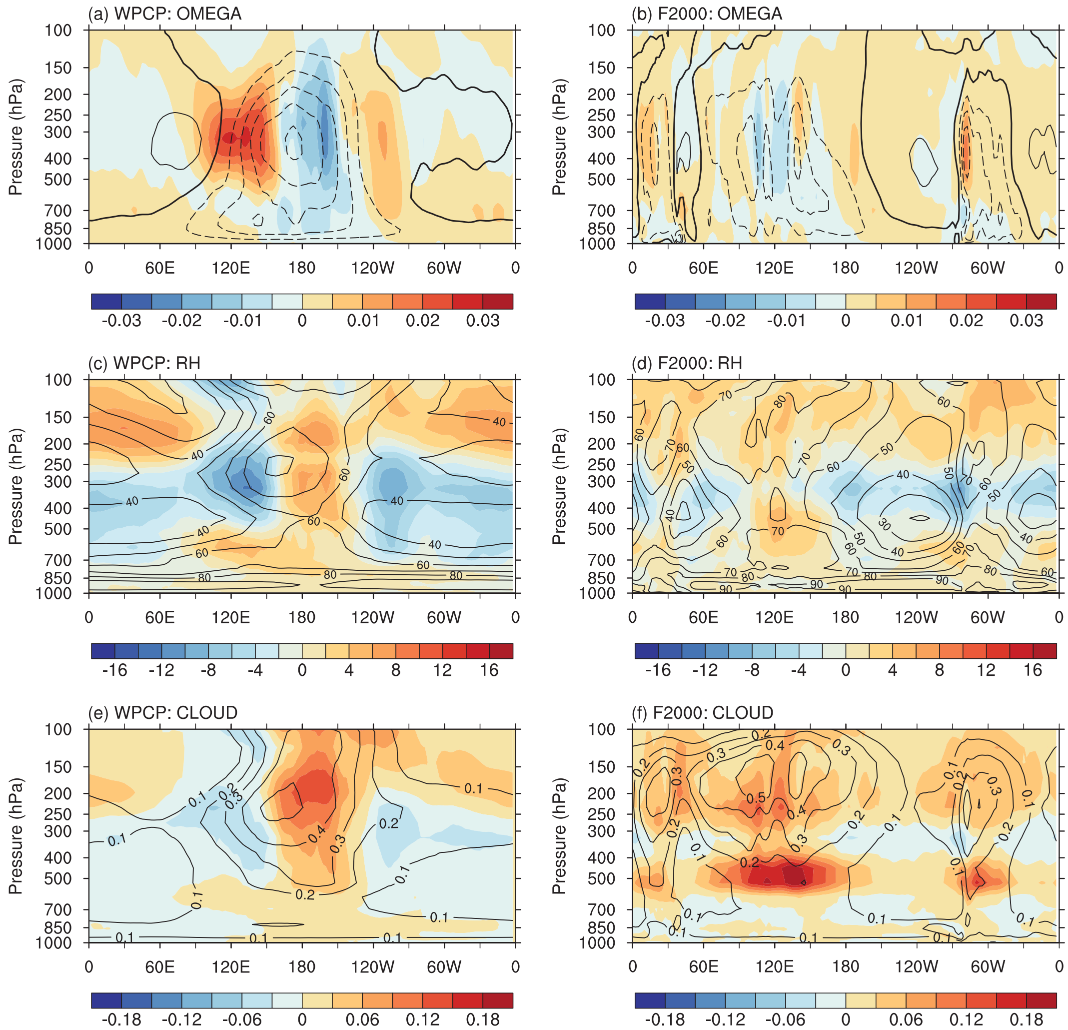

FIG. 9. (a) The difference in the vertical structure of tropical (averaged within 10°S–10°N) omega (Pa s^{-1}) between DCS500 and DCS200 in WPCP. The climatological omega of DCS200 is overlaid as contours, with a contour interval of 0.02 Pa s^{-1}. Dashed contours indicate negative values. (b) As in (a), but for F2000. (c) The difference in the vertical structure of tropical relative humidity (%) between DCS500 and DCS200 in WPCP. The climatological relative humidity of DCS200 is overlaid as contours, with a contour interval of 10%. (d) As in (c), but for F2000. (e) The difference in the vertical structure of cloud fraction between DCS500 and DCS200 in WPCP. The climatological cloud fraction of DCS200 is overlaid as contours, with a contour interval of 0.1. (f) As in (e), but for F2000.

and F2000 generate the large-scale zonal circulation. The Walker circulation (WC) is a dominant mode of equatorial zonal circulation, and its changes from DCS200 to DCS500 are shown in Fig. 10. The positive ψ_{WC} anomaly to the east of the warm pool and the negative ψ_{WC} anomaly to the west indicate that the WC strengthens under the CRE intensification in WPCP. The maximum positive and negative ψ_{WC} anomalies are located closer to the warm pool center compared to the climatological WC centers, indicating that the stronger WC contracts toward the warm pool. Similarly, in F2000, the positive ψ_{WC} anomaly over the Pacific Ocean and the negative ψ_{WC} anomaly over the Indian Ocean reflect a stronger Pacific Ocean WC and a stronger Indian Ocean WC. The Pacific Ocean WC and the Indian Ocean WC also shift toward the warm pool. The stronger WC can also be diagnosed by sea level pressure and velocity potential differences (figure not shown). In addition, the WC over the Amazon (around 80°W) weakens (Fig. 10b) in F2000. The large-scale mass compensation and the reduced surface energy fluxes (e.g., sensible and latent heat fluxes) may account for this weakening and need further investigation.

Under the CRE intensification, stronger atmospheric radiative heating over the warm pool strengthens the zonal diabatic heating gradient, driving stronger zonal overturning circulation. The strengthened upward branches of the WC support the deep convection over the warm pool, while the stronger and wider downward branches of WC strengthen the subsidence outside the warm pool, suppressing convection development there.

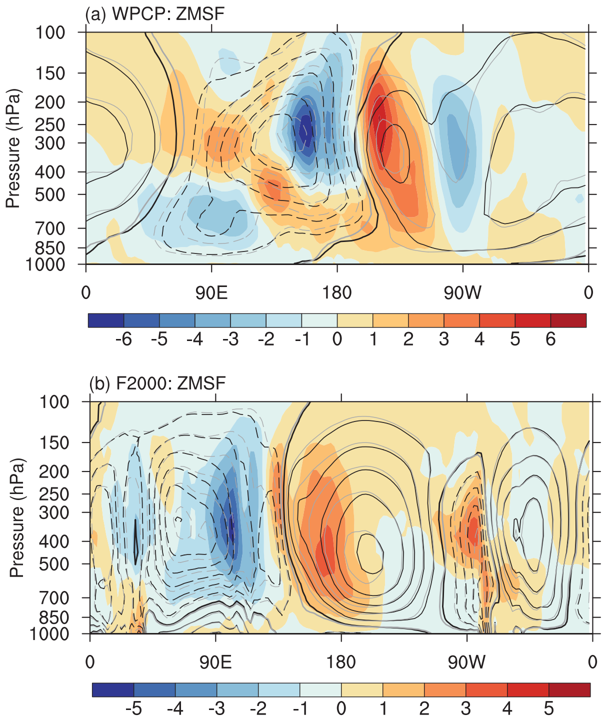

FIG. 10. (a) The difference in the climatological equatorial zonal mass streamfunction (ψ_{WC}, color; 10^{10} kg s^{-1}) between DCS500 and DCS200 in WPCP. The climatological ψ_{WC} of DCS200 (black contour) and DCS500 (gray contour) is overlaid with a contour interval of 4×10^{10} kg s^{-1}. The dashed contours indicate negative values. The positive (negative) ψ_{WC} represents the clockwise (counterclockwise) circulation. (b) As in (a), but for F2000.

2) Regional Hadley cell

Traditionally, the HC is a zonal-mean circulation over the meridional direction represented by the zonal-averaged MMSF. Many studies decompose the global HC into regional HCs (e.g., Schwendike et al. 2014; Li et al. 2023), suggesting that the regional HC exhibits different intensities and widths due to the zonally asymmetric forcings and other impact factors. In Figs. 11 and 12, the climatological regional HC is represented by the three-dimensional RMMSF, ψ_{RHC}. If the zonal average is applied to ψ_{RHC}, the vertical structure shown in Figs. 11e and 12e is close to the traditional zonal-mean HC (Figs. 3b,c), demonstrating the effectiveness of this decomposition method.

In WPCP, a strong and dominant regional HC spans a broad tropical domain and is centered near the warm pool, as indicated by the gray contour in Fig. 11a. As DCS increases, the HC exhibits significant longitudinal variations, characterized by the opposite responses of the regional HC around the warm pool and in other tropical areas. As shown in Fig. 11a, the regional HC strengthens near the warm pool under the CRE intensification, although the positive ψ_{RHC} anomaly centers are slightly displaced eastward from the SST warm pool center. In contrast, the regional HC outside the warm pool weakens or shows only minor changes. These different responses of the regional HC at different phases are further illustrated by the vertical structure of the two anomalous regional-averaged HCs, shown in Figs. 11c and 11d. Note that the selected region in Fig. 11c is not strictly defined based on the SST pattern (Fig. 1d). Instead, to better capture the strengthened regional HC dominated by the positive ψ_{RHC} anomaly in Fig. 11a, we select the region within 160°E–130°W for calculation.

Similar to WPCP, the HC in F2000 also exhibits significant regional variations with longitude when DCS increases (Fig. 12). The regional HC strengthens over the warm pool in F2000, while it weakens over the other regions, as shown by the significant ψ_{RHC} anomalies in Figs. 12a, 12c, and 12d. Note that the warm pool here is calculated based on the SST pattern (Fig. 1c).

Although the warm pool HC significantly strengthens under the CRE intensification in zonally asymmetric simulations, the zonal-mean HC still weakens overall, particularly on the equatorward flank, as presented in Fig. 3. This suggests that the weaker regional HC outside the warm pool outweighs the stronger regional HC within the warm pool, leading to a net weakening of the zonal-mean HC (detailed quantitative calculations are not shown). This underscores the importance of the regional HC changes along the zonal direction when considering global HC variations. The WPCP and F2000 simulations, with their differing model complexities, provide a robust demonstration of the regional HC's contribution to the weakening of the zonal-mean HC under CRE intensification. These results further highlight the significance of zonally asymmetric processes in HC changes, especially when compared to AQUA simulations. Although the more complex zonally asymmetric processes due to the land–sea distribution, land processes, and other related processes are simulated in F2000, the WPCP simulations exhibit similar responses. It implies that the zonally asymmetric forcings brought by the warm pool are key factors driving the opposite responses compared to AQUA when CRE strengthens, while other zonally asymmetric processes play a less pivotal role.

3) HC–WC coupling

It has been observed that there exists a coupling between the HC and WC, especially during El Niño events, despite the different mechanisms of the formation and maintenance of the HC and the WC (Yun et al. 2021). Without the ocean dynamics, the steady states of our simulation results also show the simultaneous occurrence of a weaker HC and a stronger WC under the DCS-induced CRE intensification. Therefore, the HC–WC coupling is worth further discussion.

Figure 13 shows the comparison of the circulation strength between the HC and WC in the DCS200 case. Each value for the HC is the average of the SH and NH circulation, and that for the WC is the average of the west and east circulation relative to the warm pool. The detailed values are listed in Tables C1 and C2 in appendix C. Since the WC only exists in WPCP and F2000, the values of the WC strength in AQUA are set to 0 in Fig. 13. Two different calculation methods are adopted in these calculations because the circulation centers of the HC and WC are not at the same pressure level, as shown in Figs. 3 and 10. The first method is the same as the traditional HC strength, defined in

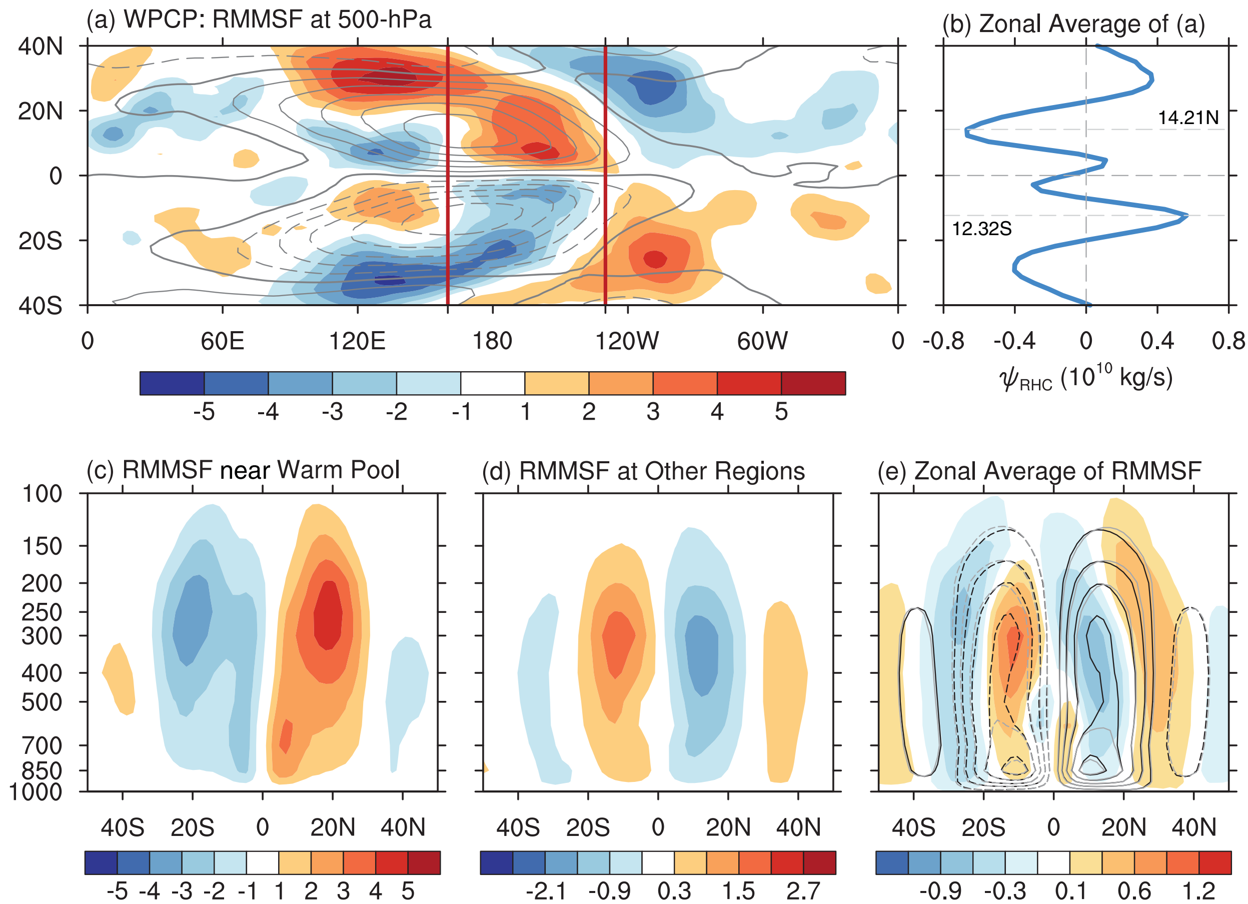

FIG. 11. (a) The difference in the climatological horizontal distribution of the regional meridional mass streamfunction (ψ_{RHC}, color; 10^{10} kg s^{-1}) at 500 hPa between DCS500 and DCS200 in WPCP. The overlaid contour with an interval of 6×10^{10} kg s^{-1} is the climatological ψ_{RHC} at 500 hPa of DCS200. The red solid lines are located at 160°E and 130°W, indicating the separation of the selected regions. (b) The zonal-averaged difference in the climatological ψ_{RHC} at 500 hPa between DCS500 and DCS200 in WPCP. The minimum and maximum of it are located at 14.21°N and 12.32°S, respectively. (c) The difference in the climatological ψ_{RHC} averaged over 160°E–130°W between DCS500 and DCS200. (d) As in (c), but averaged over other regions. (e) The zonal-averaged difference in the climatological ψ_{RHC} between DCS500 and DCS200 in WPCP, overlaid by the climatological ψ_{RHC} of DCS500 (gray contour) and DCS200 (black contour). The contour equal to zero is masked. The contour values are $(-1.2, -0.9, -0.6, -0.3, -0.1, 0.1, 0.3, 0.6, 0.9, 1.2) \times 10^{10}$ kg s^{-1}. In (a) and (c)–(e), the positive (negative) ψ_{RHC} represents the clockwise (counterclockwise) circulation, and the dashed contour indicates negative values.

section 2c, and the second method is the local maximum of the $|\psi_{HC}|$ or $|\psi_{WC}|$ near the circulation centers on the latitude-level plane or longitude-level plane. The results show that the strength of the WC is comparable to the strength of the HC in WPCP and F2000 and is even stronger than the HC, indicating that the WC is strong enough to exert an influence on the HC.

In all simulations, the higher DCS strengthens the CRE and induces stronger radiative heating over the tropics. However, in the zonally asymmetric simulations, there are zonal variations in the strength of this response, particularly with stronger radiative heating over the warm pool, which are not seen in AQUA. The stronger diabatic heating over the warm pool (or the stronger diabatic heating gradient), as a main source of the tropical thermally driven circulation, strengthens the circulation in both the meridional and zonal directions. The stronger upward branches of the WC share the same location as the upward branches of the stronger regional HC over the warm pool, supporting the upward motion and deep convection there. However, the wider and stronger downward branches of the stronger WC and their associated diabatic cooling superpose on the regional HC outside the warm pool, suppressing the ascending motion and convection over the tropics and thereby weakening the regional HC and decreasing the precipitation there. The stronger CRE intensifies the HC–WC coupling, which redistributes the atmospheric energy and reaches a new dynamic balance in the steady state.

c. *Zonal temperature gradient*

In addition to the zonally asymmetric responses discussed above, the tropical temperature response also exhibits zonal variations under CRE intensification in WPCP and F2000. In the tropical free troposphere, the weak temperature gradient

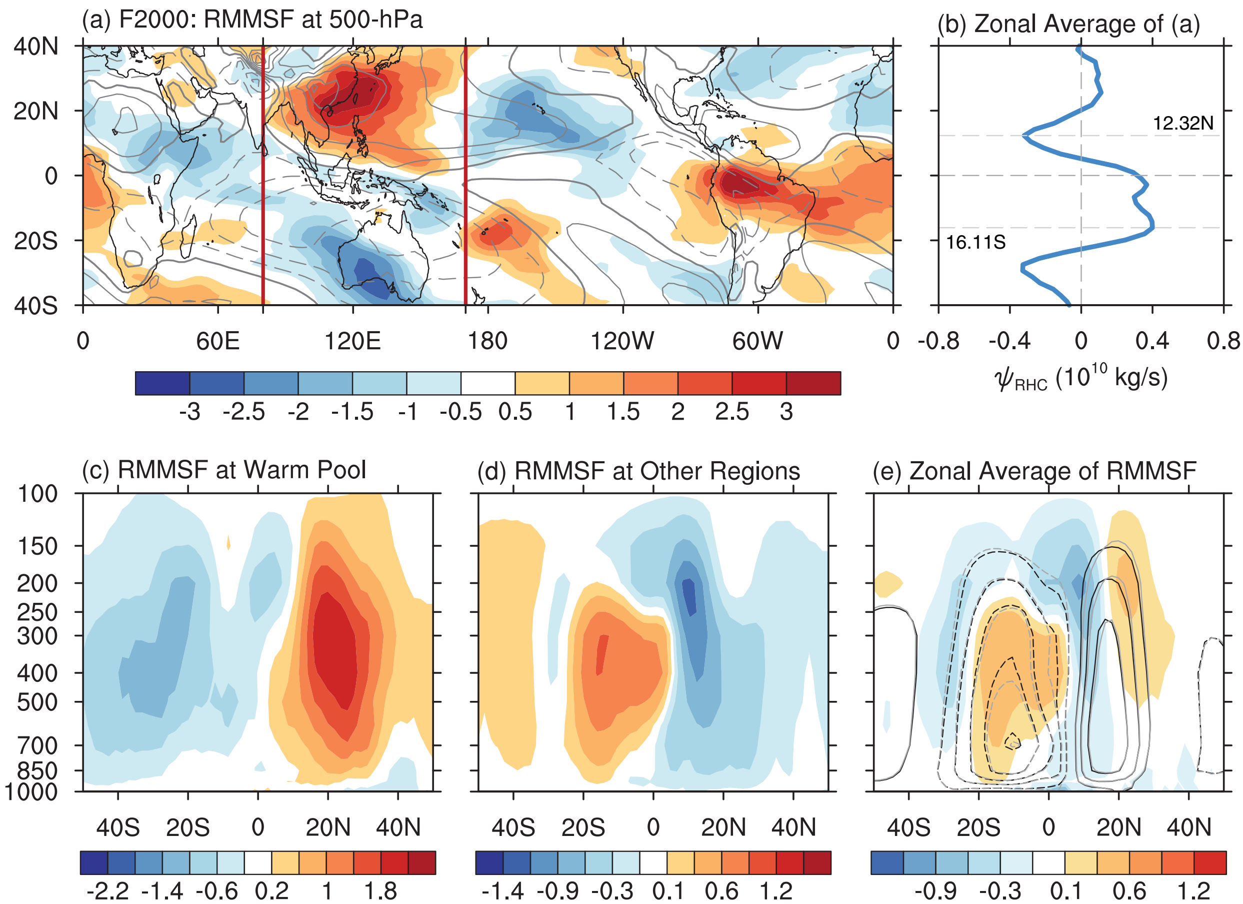

FIG. 12. As in Fig. 11, but for F2000. The red solid lines are located at 80° and 170°E in (a). The minimum and maximum of the zonal-averaged difference in the climatological ψ_{RHC} at 500 hPa between DCS500 and DCS200 are located at 12.32°N and 16.11°S, respectively, in (b). The anomalous climatological ψ_{RHC} in (c) is calculated over the warm pool (80°–170°E).

(WTG) approximation (Sobel et al. 2001) suggests that horizontal temperature gradients are typically weak. This weak horizontal temperature gradient is evident in the contours in Fig. 14. When the CRE intensifies, the tropical troposphere warms, particularly with stronger upper-tropospheric warming around the warm pool (shading in Fig. 14), strengthening the horizontal temperature gradient. Nevertheless, the upper-tropospheric temperature gradient remains very weak overall. In our fixed-SST simulations, the stronger upper-tropospheric warming around the warm pool under DCS-induced CRE intensification is potentially influenced by stronger radiative heating associated with increased cloud ice, stronger latent heating associated with stronger convection, and dynamical processes (e.g., horizontal advection and vertical motion) associated with the stronger WC (analyses not shown).

5. Conclusions and discussion

This study compares the responses of tropical precipitation and circulation to variations in cloud microphysics–induced CRE intensity in aquaplanet (AQUA) and two zonally asymmetric (WPCP and F2000) simulations using CESM2 and examines the possible causes of the simulated disparities.

When the DCS variation-induced CRE intensifies (more cloud ice and stronger LW cloud radiative forcing), the tropical mean precipitation increases, the HC strengthens, and the HC edges shift equatorward in AQUA, while the zonally asymmetric simulations display the opposite responses, with decreased tropical mean precipitation, weakened HC, and a poleward shift of the HC edges. The HC strength shows regional variations with latitudes, and the weakened HC in the zonally asymmetric simulations is predominantly contributed to by the weakened equatorward flank of the HC. Although the HC strength and edge shifts are modulated by subtropical eddy activities—mainly at the poleward flanks of the HC—the influences of subtropical eddies are insignificant over the tropics, making them not the dominant reasons for the opposite responses. Moreover, the general climate conditions cannot explain the opposite responses, since the tropical moisture and the general meridional temperature gradient respond consistently across all simulations. We therefore focus on other aspects within the tropics to elucidate the opposite precipitation and circulation responses.

Fig. 15 summarizes the potential mechanisms underlying the opposite tropical responses under the DCS-induced CRE

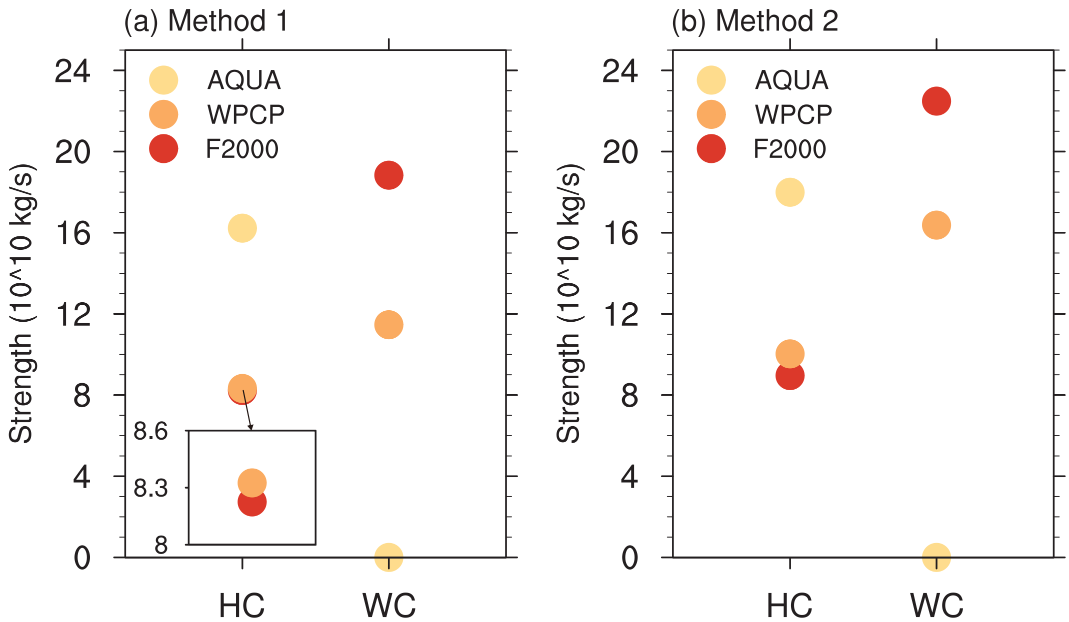

FIG. 13. The strength (10^{10} kg s^{-1}) of the HC and WC in the DCS200 case of all simulations. The strength is calculated by two different methods: (a) the maximum of $|\psi_{HC}|$ or $|\psi_{WC}|$ at 500 hPa near the circulation center; (b) the local maximum of $|\psi_{HC}|$ or $|\psi_{WC}|$ near the circulation centers on the latitude-level plane or longitude-level plane.

intensification in zonally symmetric and asymmetric simulations. In zonally symmetric AQUA, the HC strengthening and the associated increase in tropical precipitation are simply attributed to the cloud-radiative-circulation feedback induced by the stronger radiative heating over the tropics (Huang et al. 2024). By contrast, the tropical responses are more spatially complex in the zonally asymmetric simulations. The enhanced radiative heating over the warm pool induced by the DCS increase affects the zonal-mean HC and the tropical mean precipitation through two distinct pathways. First, it promotes stronger planetary-scale convective aggregation in the zonal direction: The convective region shrinks toward the warm pool, while the dry/subsidence region expands outside the warm pool, suppressing the ascending motion there. Second, the enhanced radiative heating over the warm pool strengthens the WC in the zonal direction and the regional HC in the meridional direction. The stronger and broader downward branches of the strengthened WC are superposed on the upward branches of the regional HC outside the warm pool, weakening the regional HC and suppressing the convection there. As a result, the zonal-mean HC weakens (dominated by its weakened equatorward flank) due to the stronger HC–WC coupling. Similarly, although the precipitation increases locally over the warm pool, the precipitation decreases more in the wider subsidence region outside the warm pool, leading to an overall decrease in precipitation when taking the tropical average. The comparison of our simulations also demonstrates the deterministic role of the warm pool in breaking the zonal symmetry and leading to the opposite tropical responses to the CRE intensification.

Although some results of our study appear similar to previous findings—for example, the increased precipitation over the warm pool under intensified CRE in F2000 is consistent

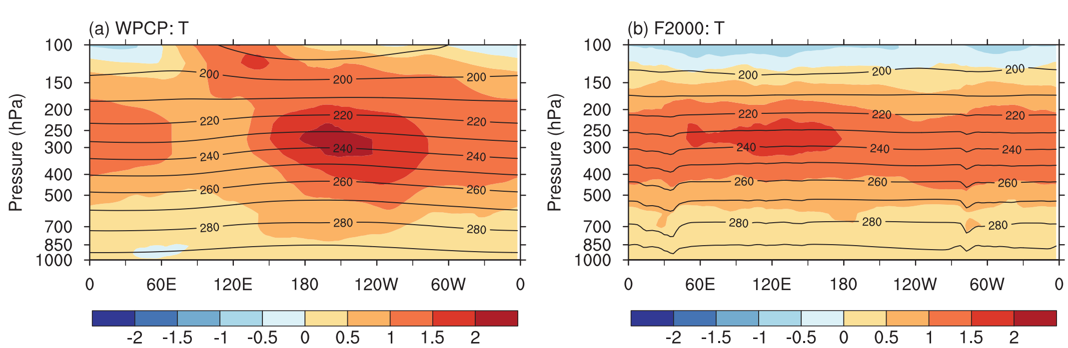

FIG. 14. (a) The difference in the vertical structure of tropical (averaged within 10°S–10°N) temperature (K) between DCS500 and DCS200 in WPCP. The climatological temperature of DCS200 is overlaid as contours. (b) As in (a), but for F2000.

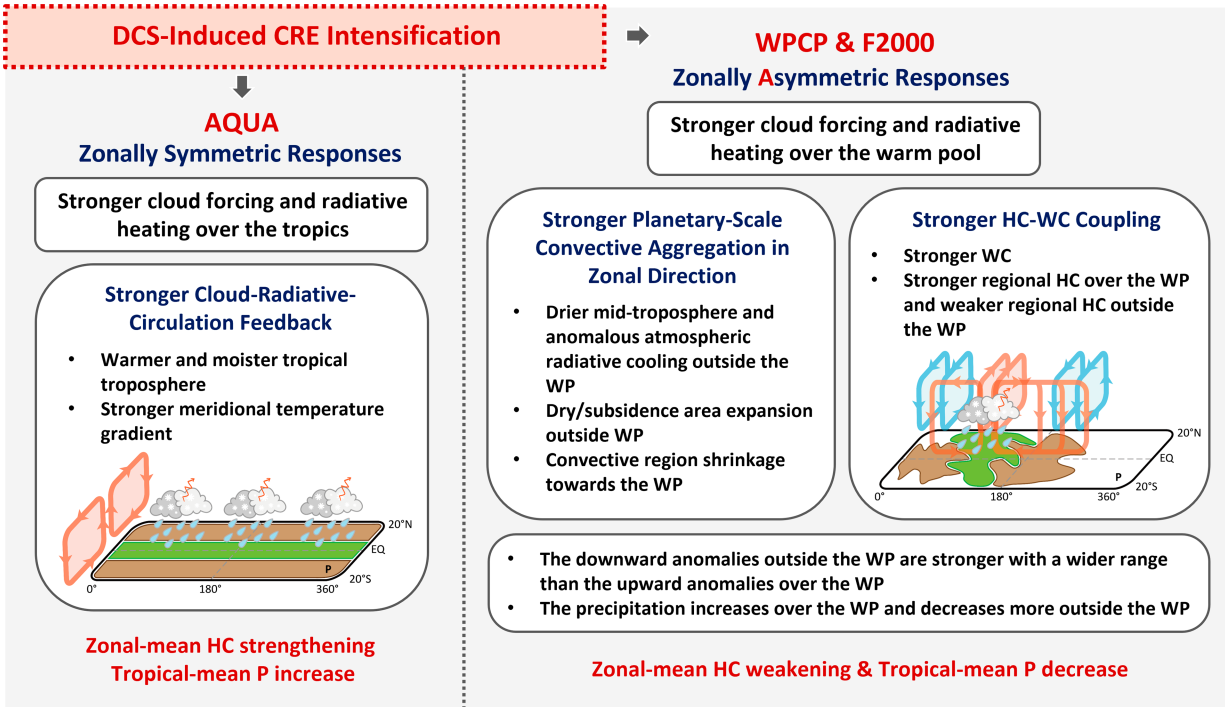

FIG. 15. A summary of the main tropical climate responses to the DCS-induced CRE change in AQUA, WPCP, and F2000. All the quantities shown in the cartoon are the differences between DCS200 and DCS500. The orange (blue) circulation represents the circulation strengthening (weakening). The green (brown) color represents the precipitation increase (decrease).

with the COOKIE experiments in AMIP-style simulations in Harrop et al. (2024)—our study offers several new insights. First, we focus on cloud microphysics-induced CRE variations, a relatively underexplored perspective in climate studies. This approach has the advantage of modulating the CRI intensity via a smoother transition, distinct from methods such as “cloud locking” or COOKIE. Simulations based on tuning the DCS not only improve our understanding of the climate impacts of CRE variations but also provide useful insights for model tuning. Second, we systematically compare the aquaplanet with two zonally asymmetric configurations as model complexity is gradually increased under CRE intensification. In particular, we include a warm-pool case, which has not been considered in previous CRE studies (e.g., Harrop and Hartmann 2016a; Medeiros et al. 2021; Harrop et al. 2024). The detailed responses in more complex simulations also complement the findings of Huang et al. (2024). Third, we highlight the qualitatively opposite responses of tropical precipitation and the HC and provide a comprehensive explanation of the possible mechanisms from different perspectives.

A previous study has found that a stronger HC is correlated with a weaker WC during El Niño events (Yun et al. 2021). Many other studies also discuss the relationship between the HC, the WC, and El Niño–Southern Oscillation (ENSO), including under global warming conditions (Lu et al. 2008; Levine and Schneider 2015). The relationship between them remains highly uncertain across various studies and still needs further investigation. Without incorporating the ocean dynamics, a weaker HC and a stronger WC occur simultaneously in the steady states of WPCP and F2000. To further explore the SST responses and the linkage between ENSO and the large-scale circulation under the DCS-induced CRE intensification, fully coupled simulations could be conducted as a test. Moreover, the steady-state SST patterns cannot fully explain the relationship between ENSO and the large-scale circulation. Future work should focus on their interannual variability.

As mentioned in section 1, future changes in the HC characteristics have been popularly discussed, and various proposed mechanisms for HC change have not reached a consensus (e.g., Chemke and Polvani 2021). Most previous studies focus on the zonal-mean conditions (e.g., temperature, tropopause height, static stability) and meridional processes that drive HC dynamics, rather than considering the impacts of longitudinal variations. Our study emphasizes that—beyond the classic theories explaining the mechanisms of HC changes, for example, the meridional temperature and diabatic heating gradient—the coupling of the HC with the zonal circulation and the regional differences in the HC associated with the zonal asymmetry may also warrant attention. These zonal asymmetric responses cannot be captured by the zonal-mean patterns, supplementing our understanding of HC variations.

Acknowledgments. We thank the three anonymous reviewers for their constructive comments and suggestions, which helped improve the quality and clarity of this manuscript. The work described in this paper was substantially supported by Grant AoE/P-601/23-N from the Research Grants Council (RGC) of the Hong Kong Special Administrative Region, China. X. S. was additionally supported by R. G. C. Grant HKUST-16301322 and the Center for Ocean Research in Hong Kong and Macau (CORE), a joint research center between the Laoshan Laboratory of Science and Technology and the Hong Kong University of Science and Technology (HKUST). D. K. was funded by the Creative-Pioneering Researchers Program from Seoul National University, the National Research Foundation of Korea (NRF) grant funded by the Korea government (MSIT) (RS-2024-00336160), and the Korea Meteorological Administration Research and Development Program under Grant (RS-2025-02221669). T. M. was supported by the JSPS KAKENHI Grants 22H01297/23K22568, 24K00707, and 24H02228. The authors thank HKUST Fok Ying Tung Research Institute and the National Supercomputing Center in Guangzhou Nansha subcenter for providing high-performance computational resources.

Data availability statement. The description, installation, and other information about CESM2 can be found on the web page: https://www.cesm.ucar.edu/models/cesm2/. The simulation data for figure plotting are available on Zenodo (Huang 2024).

APPENDIX A

Regionally Averaged Precipitation

The regionally averaged precipitation for the three cases and the fractional changes are shown in Tables A1 and A2.

TABLE A1. The precipitation (mm day^{-1}, the unit is not shown in the table) averaged over 10°S–10°N and its fractional change (%) from DCS200 to DCS500.

	AQUA	WPCP	F2000
DCS200	7.49	5.66	5.00
DCS500	8.47	5.49	4.81
Fractional change	+13.08%	−3.00%	−3.80%

TABLE A2. As in Table A1, but for the precipitation averaged over 5°S–5°N.

	AQUA	WPCP	F2000
DCS200	7.08	6.00	4.76
DCS500	9.46	5.93	4.57
Fractional change	+33.62%	−1.17%	−3.99%

APPENDIX B

Spatial Distribution of Atmospheric Radiative Forcing Responses

The spatial distributions of the atmospheric radiative forcing responses to CRE intensification in Fig. 8 are decomposed into cloud and clear-sky components, as shown in Fig. B1.

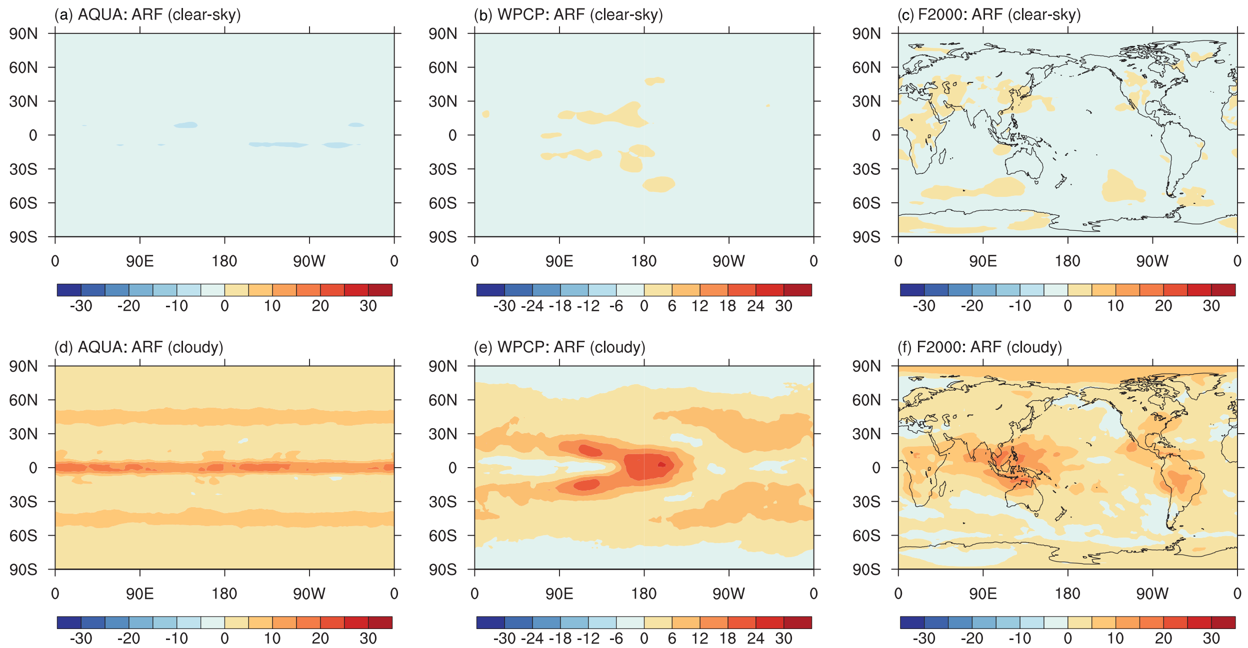

FIG. B1. (a) The difference in the climatological clear-sky atmospheric radiative forcing (color; W m^{-2}) between DCS500 and DCS200 in AQUA. (b) As in (a), but for WPCP. (c) As in (a), but for F2000. (d)–(f) As in (a)–(c), but for the cloud component. The positive values indicate the radiative heating anomaly.

APPENDIX C

Strength of the Hadley Cell and Walker Circulation

The strength of the HC and WC in each hemisphere in the DCS200 case across all simulations is shown in Tables C1 and TC2. Two calculation methods are adopted.

TABLE C1. The strength of the HC (10^{10} kg s^{-1}) in DCS200 cases of all simulations. The values on the left are calculated by the maximum of ψ_{HC} at 500 hPa near the HC center. The values on the right are calculated by the local maximum of ψ_{HC} near the HC center on the latitude-level plane.

	AQUA	WPCP	F2000
SH	16.23/17.98	8.36/9.98	9.21/10.52
NH	16.22/18.01	8.29/10.08	7.24/7.40

TABLE C2. The strength of the WC (10^{10} kg s^{-1}) in DCS200 cases of zonally asymmetric simulations. The values on the left are calculated by the maximum of ψ_{WC} at 500 hPa near the WC center. The values on the right are calculated by the local maximum of ψ_{WC} near the WC center on the longitude-level plane.

	WPCP	F2000
West	13.72/22.77	17.21/24.18
East	9.21/9.98	20.46/20.79

REFERENCES

Allen, M. R., and W. J. Ingram, 2002: Constraints on future changes in climate and the hydrologic cycle. *Nature*, **419**, 224–232, https://doi.org/10.1038/nature01092.

Arnold, N. P., and D. A. Randall, 2015: Global-scale convective aggregation: Implications for the Madden-Julian Oscillation. *J. Adv. Model. Earth Syst.*, **7**, 1499–1518, https://doi.org/10.1002/2015MS000498.

Bogenschutz, P. A., A. Gettelman, H. Morrison, V. E. Larson, C. Craig, and D. P. Schanen, 2013: Higher-order turbulence closure and its impact on climate simulations in the Community Atmosphere Model. *J. Climate*, **26**, 9655–9676, https://doi.org/10.1175/JCLI-D-13-00075.1.

Ceppi, P., and D. L. Hartmann, 2015: Connections between clouds, radiation, and midlatitude dynamics: A review. *Curr. Climate Change Rep.*, **1**, 94–102, https://doi.org/10.1007/s40641-015-0010-x.

Chemke, R., and L. M. Polvani, 2021: Elucidating the mechanisms responsible for Hadley cell weakening under 4 × CO_2 forcing. *Geophys. Res. Lett.*, **48**, e2020GL090348, https://doi.org/10.1029/2020GL090348.

——, ——, and C. Deser, 2019: The effect of Arctic sea ice loss on the Hadley circulation. *Geophys. Res. Lett.*, **46**, 963–972, https://doi.org/10.1029/2018GL081110.

Chen, Y.-J., Y.-T. Hwang, and P. Ceppi, 2021: The impacts of cloud-radiative changes on poleward atmospheric and oceanic energy transport in a warmer climate. *J. Climate*, **34**, 7857–7874, https://doi.org/10.1175/JCLI-D-20-0949.1.

Eidhammer, T., H. Morrison, A. Bansemer, A. Gettelman, and A. J. Heymsfield, 2014: Comparison of ice cloud properties simulated by the Community Atmosphere Model (CAM5) with in-situ observations. *Atmos. Chem. Phys.*, **14**, 10 103–10 118, https://doi.org/10.5194/acp-14-10103-2014.

——, ——, D. Mitchell, A. Gettelman, and E. Erfani, 2017: Improvements in global climate model microphysics using a consistent representation of ice particle properties. *J. Climate*, **30**, 609–629, https://doi.org/10.1175/JCLI-D-16-0050.1.

Fan, Y., Y. T. Chung, and X. Shi, 2021: The essential role of cloud-radiation interaction in nonrotating convective self-aggregation. *Geophys. Res. Lett.*, **48**, e2021GL095102, https://doi.org/10.1029/2021GL095102.

Gettelman, A., and H. Morrison, 2015: Advanced two-moment bulk microphysics for global models. Part I: Off-line tests and comparison with other schemes. *J. Climate*, **28**, 1268–1287, https://doi.org/10.1175/JCLI-D-14-00102.1.

Golaz, J.-C., V. E. Larson, and W. R. Cotton, 2002: A PDF-based model for boundary layer clouds. Part I: Method and model description. *J. Atmos. Sci.*, **59**, 3540–3551, https://doi.org/10.1175/1520-0469(2002)059<3540:APBMFB>2.0.CO;2.

Harrop, B. E., and D. L. Hartmann, 2016a: The role of cloud radiative heating in determining the location of the ITCZ in aquaplanet simulations. *J. Climate*, **29**, 2741–2763, https://doi.org/10.1175/JCLI-D-15-0521.1.

——, and ——, 2016b: The role of cloud radiative heating within the atmosphere on the high cloud amount and top-of-atmosphere cloud radiative effect. *J. Adv. Model. Earth Syst.*, **8**, 1391–1410, https://doi.org/10.1002/2016MS000670.

——, and Coauthors, 2024: An overview of cloud–radiation denial experiments for the Energy Exascale Earth System Model version 1. *Geosci. Model Dev.*, **17**, 3111–3135, https://doi.org/10.5194/gmd-17-3111-2024.

Hartmann, D. L., and D. A. Short, 1980: On the use of earth radiation budget statistics for studies of clouds and climate. *J. Atmos. Sci.*, **37**, 1233–1250, https://doi.org/10.1175/1520-0469(1980)037<1233:OTUOER>2.0.CO;2.

Hu, Y., H. Huang, and C. Zhou, 2018: Widening and weakening of the Hadley circulation under global warming. *Sci. Bull.*, **63**, 640–644, https://doi.org/10.1016/j.scib.2018.04.020.

Huang, Y., 2024: Dataset for "How do tropical precipitation and circulations respond to the cloud-radiative effect changes?". Zenodo, accessed 20 April 2026, https://doi.org/10.5281/zenodo.12071105.

——, D. Kim, T. Zhou, and X. Shi, 2024: The role of cloud-radiative interaction in tropical circulation and the Madden–Julian oscillation. *J. Climate*, **37**, 4559–4576, https://doi.org/10.1175/JCLI-D-23-0736.1.

Hwang, Y.-T., and D. M. W. Frierson, 2013: Link between the double-Intertropical Convergence Zone problem and cloud biases over the Southern Ocean. *Proc. Natl. Acad. Sci. USA*, **110**, 4935–4940, https://doi.org/10.1073/pnas.1213302110.

Iacono, M. J., J. S. Delamere, E. J. Mlawer, M. W. Shephard, S. A. Clough, and W. D. Collins, 2008: Radiative forcing by long-lived greenhouse gases: Calculations with the AER radiative transfer models. *J. Geophys. Res.*, **113**, D13103, https://doi.org/10.1029/2008JD009944.

Kim, D., M.-S. Ahn, I.-S. Kang, and A. D. Del Genio, 2015: Role of longwave cloud–radiation feedback in the simulation of the Madden–Julian oscillation. *J. Climate*, **28**, 6979–6994, https://doi.org/10.1175/JCLI-D-14-00767.1.

——, H. Kim, S. M. Kang, M. F. Stuecker, and T. M. Merlis, 2022: Weak Hadley cell intensity changes due to compensating effects of tropical and extratropical radiative forcing. *npj Climate Atmos. Sci.*, **5**, 61, https://doi.org/10.1038/s41612-022-00287-x.

Kim, S.-Y., and Coauthors, 2023: Hemispherically asymmetric Hadley cell response to CO_2 removal. *Sci. Adv.*, **9**, eadg1801, https://doi.org/10.1126/sciadv.adg1801.

Lebsock, M. D., C. Kummerow, and G. L. Stephens, 2010: An observed tropical oceanic radiative–convective cloud feedback. *J. Climate*, **23**, 2065–2078, https://doi.org/10.1175/2009JCLI3091.1.

Levine, X. J., and T. Schneider, 2011: Response of the Hadley circulation to climate change in an aquaplanet GCM coupled to a simple representation of ocean heat transport. *J. Atmos. Sci.*, **68**, 769–783, https://doi.org/10.1175/2010JAS3553.1.

——, and ——, 2015: Baroclinic eddies and the extent of the Hadley circulation: An idealized GCM study. *J. Atmos. Sci.*, **72**, 2744–2761, https://doi.org/10.1175/JAS-D-14-0152.1.

Li, Y., D. W. J. Thompson, and S. Bony, 2015: The influence of atmospheric cloud radiative effects on the large-scale atmospheric circulation. *J. Climate*, **28**, 7263–7278, https://doi.org/10.1175/JCLI-D-14-00825.1.

——, and Coauthors, 2023: Interannual variability of regional Hadley circulation and El Niño interaction. *Geophys. Res. Lett.*, **50**, e2022GL102016, https://doi.org/10.1029/2022GL102016.

Lu, J., G. Chen, and D. M. W. Frierson, 2008: Response of the zonal mean atmospheric circulation to El Niño versus global warming. *J. Climate*, **21**, 5835–5851, https://doi.org/10.1175/2008JCLI2200.1.

Medeiros, B., D. L. Williamson, and J. G. Olson, 2016: Reference aquaplanet climate in the Community Atmosphere Model, Version 5. *J. Adv. Model. Earth Syst.*, **8**, 406–424, https://doi.org/10.1002/2015MS000593.

——, A. C. Clement, J. J. Benedict, and B. Zhang, 2021: Investigating the impact of cloud-radiative feedbacks on tropical precipitation extremes. *npj Climate Atmos. Sci.*, **4**, 18, https://doi.org/10.1038/s41612-021-00174-x.

Middlemas, E. A., A. C. Clement, B. Medeiros, and B. Kirtman, 2019: Cloud radiative feedbacks and El Niño–Southern Oscillation. *J. Climate*, **32**, 4661–4680, https://doi.org/10.1175/JCLI-D-18-0842.1.

Morrison, H., and A. Gettelman, 2008: A new two-moment bulk stratiform cloud microphysics scheme in the Community Atmosphere Model, version 3 (CAM3). Part I: Description and numerical tests. *J. Climate*, **21**, 3642–3659, https://doi.org/10.1175/2008JCLI2105.1.

Quan, H., B. Zhang, C. Wang, and S. Fueglistaler, 2025: The sea surface temperature pattern effect on outgoing longwave radiation: The role of large-scale convective aggregation. *Geophys. Res. Lett.*, **52**, e2024GL112756, https://doi.org/10.1029/2024GL112756.

Ruppert, J. H., A. A. Wing, X. Tang, and E. L. Duran, 2020: The critical role of cloud–infrared radiation feedback in tropical cyclone development. *Proc. Natl. Acad. Sci. USA*, **117**, 27 884–27 892, https://doi.org/10.1073/pnas.2013584117.

Schiro, K. A., and Coauthors, 2022: Model spread in tropical low cloud feedback tied to overturning circulation response to warming. *Nat. Commun.*, **13**, 7119, https://doi.org/10.1038/s41467-022-34787-4.

Schneider, T., and S. Bordoni, 2008: Eddy-mediated regime transitions in the seasonal cycle of a Hadley circulation and implications for monsoon dynamics. *J. Atmos. Sci.*, **65**, 915–934, https://doi.org/10.1175/2007JAS2415.1.

Schwendike, J., P. Govekar, M. J. Reeder, R. Wardle, G. J. Berry, and C. Jakob, 2014: Local partitioning of the overturning circulation in the tropics and the connection to the Hadley and Walker circulations. *J. Geophys. Res. Atmos.*, **119**, 1322–1339, https://doi.org/10.1002/2013JD020742.

Seo, K.-H., D. M. W. Frierson, and J.-H. Son, 2014: A mechanism for future changes in Hadley circulation strength in CMIP5 climate change simulations. *Geophys. Res. Lett.*, **41**, 5251–5258, https://doi.org/10.1002/2014GL060868.

——, S.-P. Yoon, J. Lu, Y. Hu, P. W. Staten, and D. M. W. Frierson, 2023: What controls the interannual variation of Hadley cell extent in the Northern Hemisphere: Physical mechanism and empirical model for edge variation. *npj Climate Atmos. Sci.*, **6**, 204, https://doi.org/10.1038/s41612-023-00533-w.

Shaw, T. A., 2019: Mechanisms of future predicted changes in the zonal mean mid-latitude circulation. *Curr. Climate Change Rep.*, **5**, 345–357, https://doi.org/10.1007/s40641-019-00145-8.

Shi, X., D. Kim, Á. F. Adames, and J. Sukhatme, 2018: WISHE-moisture mode in an aquaplanet simulation. *J. Adv. Model. Earth Syst.*, **10**, 2393–2407, https://doi.org/10.1029/2018MS001441.

Sobel, A. H., J. Nilsson, and L. M. Polvani, 2001: The weak temperature gradient approximation and balanced tropical moisture waves. *J. Atmos. Sci.*, **58**, 3650–3665, https://doi.org/10.1175/1520-0469(2001)058<3650:TWTGAA>2.0.CO;2.

Stephens, G. L., and T. D. Ellis, 2008: Controls of global-mean precipitation increases in global warming GCM experiments. *J. Climate*, **21**, 6141–6155, https://doi.org/10.1175/2008JCLI2144.1.

Stevens, B., S. Bony, and M. Webb, 2012: Clouds On-Off Klimate Intercomparison Experiment (COOKIE). EUCLIPSE Tech. Rep., 12 pp.

Tobin, I., S. Bony, and R. Roca, 2012: Observational evidence for relationships between the degree of aggregation of deep convection, water vapor, surface fluxes, and radiation. *J. Climate*, **25**, 6885–6904, https://doi.org/10.1175/JCLI-D-11-00258.1.

——, ——, C. E. Holloway, J.-Y. Grandpeix, G. Sèze, D. Coppin, S. J. Woolnough, and R. Roca, 2013: Does convective aggregation need to be represented in cumulus parameterizations? *J. Adv. Model. Earth Syst.*, **5**, 692–703, https://doi.org/10.1002/jame.20047.

Voigt, A., N. Albern, P. Ceppi, K. Grise, Y. Li, and B. Medeiros, 2021: Clouds, radiation, and atmospheric circulation in the present-day climate and under climate change. *WIREs Climate Change*, **12**, e694, https://doi.org/10.1002/wcc.694.

Walker, C. C., and T. Schneider, 2006: Eddy influences on Hadley circulations: Simulations with an idealized GCM. *J. Atmos. Sci.*, **63**, 3333–3350, https://doi.org/10.1175/JAS3821.1.

Williamson, L., and Coauthors, 2012: The APE Atlas. NCAR Tech. Note NCAR/TN-484+STR, 532 pp., https://doi.org/10.5065/D6FF3QBR.

Yu, B., and F. W. Zwiers, 2010: Changes in equatorial atmospheric zonal circulations in recent decades. *Geophys. Res. Lett.*, **37**, L05701, https://doi.org/10.1029/2009GL042071.

Yun, K.-S., A. Timmermann, and M. F. Stuecker, 2021: Synchronized spatial shifts of Hadley and Walker circulations. *Earth Syst. Dyn.*, **12**, 121–132, https://doi.org/10.5194/esd-12-121-2021.

Zhang, G., and Z. Wang, 2013: Interannual variability of the Atlantic Hadley circulation in boreal summer and its impacts on tropical cyclone activity. *J. Climate*, **26**, 8529–8544, https://doi.org/10.1175/JCLI-D-12-00802.1.

——, and ——, 2015: Interannual variability of tropical cyclone activity and regional Hadley circulation over the northeastern Pacific. *Geophys. Res. Lett.*, **42**, 2473–2481, https://doi.org/10.1002/2015GL063318.

Zhang, G. J., and N. A. McFarlane, 1995: Sensitivity of climate simulations to the parameterization of cumulus convection in the Canadian Climate Centre general circulation model. *Atmos.–Ocean*, **33**, 407–446, https://doi.org/10.1080/07055900.1995.9649539.

Zhang, L., Y. Huang, M. Lu, and X. Shi, 2025: Impact of cloud radiative forcing on tropical cyclone frequency and intensity through tuning the cloud ice-to-snow diameter threshold. *Environ. Res. Lett.*, **20**, 014027, https://doi.org/10.1088/1748-9326/ad9b3c.

Zhao, C., and Coauthors, 2013: A sensitivity study of radiative fluxes at the top of atmosphere to cloud-microphysics and aerosol parameters in the Community Atmosphere Model CAM5. *Atmos. Chem. Phys.*, **13**, 10 969–10 987, https://doi.org/10.5194/acp-13-10969-2013.